P-to-S and S-to-P imaging of a sharp lithosphere-asthenosphere boundary beneath eastern North America

Catherine A. Rychert,[1,2] Stéphane Rondenay,[3] and Karen M. Fischer[1]

[1]   S-to-P (Sp) scattered energy independently confirms the existence of a seismic velocity discontinuity at the lithosphere-asthenosphere boundary that was previously imaged using P-to-S (Ps) scattered energy in eastern North America. Exploration of the different sensitivities of Ps and Sp scattered energy suggests that the phases contain independent yet complementary high-resolution information regarding velocity contrasts. Combined inversions of Ps and Sp energy have the potential to tightly constrain associated velocity gradients. In eastern North America, inversions of Sp and Ps data require a strong, 5–10% velocity contrast that is also sharp, occurring over less than 11 km at 87–105 km depth. Thermal gradients alone are insufficient to create such a sharp boundary, and therefore another mechanism is required. A boundary in composition, hydration, or a change in anisotropic signature could easily produce a sufficiently localized velocity gradient. Taken separately, the magnitudes of the effects of these mechanisms are too small to match our observed velocity gradients. However, our observations may be explained by a boundary in hydration coupled with a boundary in depletion and/or anisotropy. Alternatively, a small amount of melt in the asthenosphere could explain the velocity gradient. The tight constraints on velocity gradients achieved by combined modeling of Ps and Sp energy offer promise for defining the character of the lithosphere-asthenosphere boundary globally.

1. Introduction

[2]   To understand what makes a tectonic plate "plate-like," the lithosphere-asthenosphere boundary must be investigated globally through detailed local and regional studies that span different tectonic environments. In particular, the seismic gradient associated with the boundary must be constrained to determine the physical and chemical properties that define the boundary. In this study we focus on a region of eastern North America where previous P-to-S (Ps) imaging [*Rychert et al.*, 2005] located a velocity drop at depths consistent with the base of the seismically fast lithospheric lid [*Li et al.*, 2003; *van der Lee*, 2002]. The high-resolution capabilities of Ps inversions provided tight constraints on the sharpness of the velocity gradient, requiring a 3.1–11% velocity drop that occurs over 11 km or less. These results narrow the range of possible physical and chemical mechanisms that may define the boundary. For instance, the lithosphere-asthenosphere gradient in

eastern North America is too sharp to be defined by thermal gradients alone [*Rychert et al.*, 2005]. In this study we further examine the properties of the lithosphere-asthenosphere boundary in this region by exploring the new information provided by combined analysis of Ps and S-to-P (Sp) phases.

[3]   Although a discontinuity associated with the lithosphere-asthenosphere boundary has not been observed globally [*Shearer*, 1991], relatively sharp velocity gradients have been observed regionally using a variety of methods. Discontinuities associated with a transition from a fast seismic lid to a deeper, slower low-velocity zone have been observed by several reflection and refraction experiments [*MONA LISA Working Group*, 1997; *Morozova et al.*, 1999; *Ryberg et al.*, 1996; *Steer et al.*, 1998a, 1998b; *Thybo and Perchuc*, 1997]. Regional imaging of discontinuities in the lithosphere-asthenosphere boundary depth range has also been accomplished using reflected teleseismic body wave phases [*Revenaugh and Jordan*, 1991; *Revenaugh and Sipkin*, 1994], and recently, progress has been made using Ps and Sp scattered phases [*Bostock*, 1998; *Chen et al.*, 2006; *Collins et al.*, 2001; *Farra and Vinnik*, 2000; *Kumar et al.*, 2005a, 2005b, 2006; *Li et al.*, 2000, 2004; *Mohsen et al.*, 2006; *Oreshin et al.*, 2002; *Rychert et al.*, 2005; *Sodoudi et al.*, 2006; *Vinnik and Farra*, 2002; *Vinnik et al.*, 2003, 2004a, 2004b, 2005b].

[4]   One of the advantages of using Sp instead of Ps phases to consider deeper discontinuities such as the lithosphere-asthenosphere boundary is that Sp imaging avoids

[1]Department of Geological Sciences, Brown University, Providence, Rhode Island, USA.
[2]Now at Institute of Geophysics and Planetary Physics, Scripps Institution of Oceanography, University of California, San Diego, La Jolla, California, USA.
[3]Department of Earth, Atmospheric, and Planetary Sciences, Massachusetts Institute of Technology, Cambridge, Massachusetts, USA.
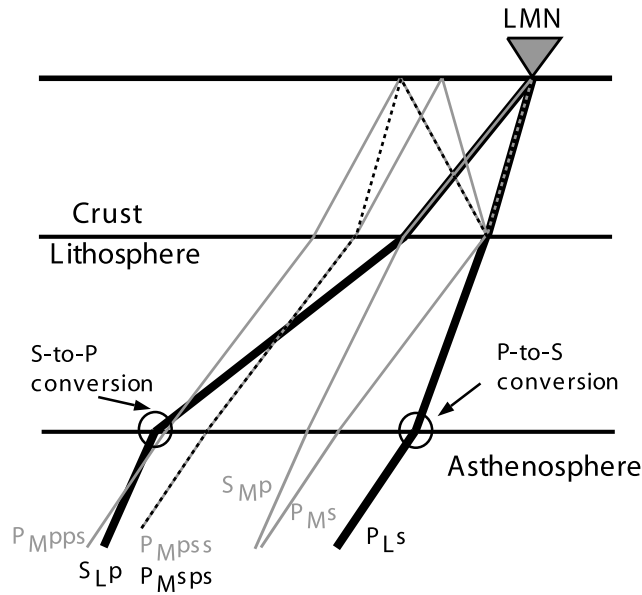
Figure 1. *Ps* and *Sp* raypaths. Raypaths of the direct *Ps* and *Sp* phases and the first-order *Ps* reverberations are shown. Thick black lines show the raypaths of *Ps* ($P_L s$) and *Sp* ($S_L p$) direct conversions from the base of the lithosphere. Grey lines indicate the *Ps* ($P_M s$) and *Sp* ($S_M p$) direct conversions from the Moho, and the first-order *Ps* reverberations that also appear in the data: $P_M pps$, $P_M pss$, and $P_M sps$ (dashed black line for clarity). Note that $P_M pss$ and $P_M sps$ arrive simultaneously.

complications due to reverberations from shallower discontinuities which are present in *Ps* data [*Kumar et al.*, 2005b; *Oreshin et al.*, 2002; *Vinnik and Farra*, 2002; *Vinnik et al.*, 2003, 2004a, 2005b]. In *Ps* imaging, both the direct conversion from a discontinuity as well as the phases which reverberate between the discontinuity and the surface arrive after the incident *P* wave, with the reverberations arriving later than the direct conversion (Figure 1). In *Sp* imaging, reverberations are avoided because reverberations and direct conversions are completely separated, the former arriving after the incident *S* wave, and the latter arriving before the incident *S* wave.

[5] *Sp* imaging has illuminated decreases in velocity with depth beneath several continental regions, including the Southwest German Basin (80 km depth) [*Farra and Vinnik*, 2000], the Dabie Shan in central eastern China (60–72 km depth) [*Sodoudi et al.*, 2006], the region from the Dead Sea Transform (65–80 km depth) to eastern Turkey (90 km depth) and the Arabian Shield (160 km depth) [*Mohsen et al.*, 2006], the central Himalayan-Tibetan orogen (160–220 km depth) [*Kumar et al.*, 2006], and the region from the Tien Shan orogenic belt (90–120 km depth) to the Pamir and Karakoram orogenic belts (120–270 km) [*Kumar et al.*, 2005b; *Oreshin et al.*, 2002; *Vinnik et al.*, 2004b]. *Sp* imaging has also been used to infer the lithosphere-asthenosphere boundary in hot spot regions, for example beneath Hawaii [*Li et al.*, 2004] and Iceland, Greenland and Jan Mayen at depths that vary from 40–60 km to 100–120 km [*Kumar et al.*, 2005a; *Vinnik et al.*, 2005b].

[6] *Sp* phases have also been modeled to determine the magnitude and sharpness of the associated velocity gradient.

Where a discontinuity in the 50–160 km depth range has been imaged using *Sp* scattered energy and the velocity gradient has also been modeled, the gradient has been strong, 6.9–8.9% [*Oreshin et al.*, 2002; *Vinnik et al.*, 2004a, 2005b], and as sharp as 21 km [*Vinnik et al.*, 2005b].

[7] In the locations where *Ps* imaging and *Sp* imaging have both been performed, *Sp* imaging has served to independently confirm the existence of discontinuities which were observed in *Ps* data [*Farra and Vinnik*, 2000; *Li et al.*, 2000, 2004; *Sodoudi et al.*, 2006; *Vinnik et al.*, 2004b; *Yuan et al.*, 2006]. In this study we invert both *Sp* and *Ps* data to exploit the independent, yet complementary information contained in the phases. Such combined analysis has the potential to tightly constrain the velocity gradient associated with the base of the lithosphere, and thus the physical and chemical properties that define the boundary.

[8] Our study region spans the Paleozoic Appalachian orogen and the eastern coastal margin of the United States (Figure 2). Following the collision of the proto-African and proto-North American plates, the last major tectonic events to affect the lithosphere in this area were Triassic and Jurassic rifting in the east related to the opening of the Atlantic Ocean [*Hatcher*, 1989], and passage of the lithosphere over a plume ∼100–120 Myr ago [*Heaman and Kjarsgaard*, 2000].

[9] Lithosphere-asthenosphere boundary investigations in this region include our *Ps* study which images a seismic velocity discontinuity at 90–110 km depth that dips gradually northwest [*Rychert et al.*, 2005]. Surface wave studies also image a seismically fast lithospheric lid in eastern North America that extends to roughly 200 km depth beneath the craton just to the west of our study region, and thins to 80–90 km depth at the continental margin in the east [*Li et al.*, 2003; *van der Lee*, 2002].

[10] Here we confirm the existence of a discontinuity associated with the lithosphere-asthenosphere boundary in eastern North America. We also invert the *Sp* data from the same stations that were used in *Ps* inversions, and combine our results with a new, expanded set of *Ps* inversions to explore the sensitivity of the two phases. This analysis allows us to verify previous inversion results, to place tighter constraints on the associated velocity gradient, and to further explore the mechanisms required to explain the sharp velocity gradient.

2. Data and Imaging

2.1. Data

[11] We focus on describing the *Sp* data here since the *Ps* data and much of the *Ps* modeling has already been published [*Rychert et al.*, 2005]. In the *Sp* analysis, we analyze the *SV* and *P* components from our best stations in eastern North America, HRV and LMN (Figures 3c and 3d). The stations have been operating for over 10 years, and we model data recorded at the two stations between 1988–2002 and 1993–2003, respectively. We focus on our best two stations because *Sp* imaging requires higher data quality than *Ps* imaging due to greater noise content in *Sp* waveforms. In *Sp* imaging it is also necessary to avoid possible inference with unwanted phases such as *SKS*, *pPPP*, *pPPPP*, and *sPPPP* [*Wilson et al.*, 2006]. We minimize interference from these phases by rejecting events from depths >300 km
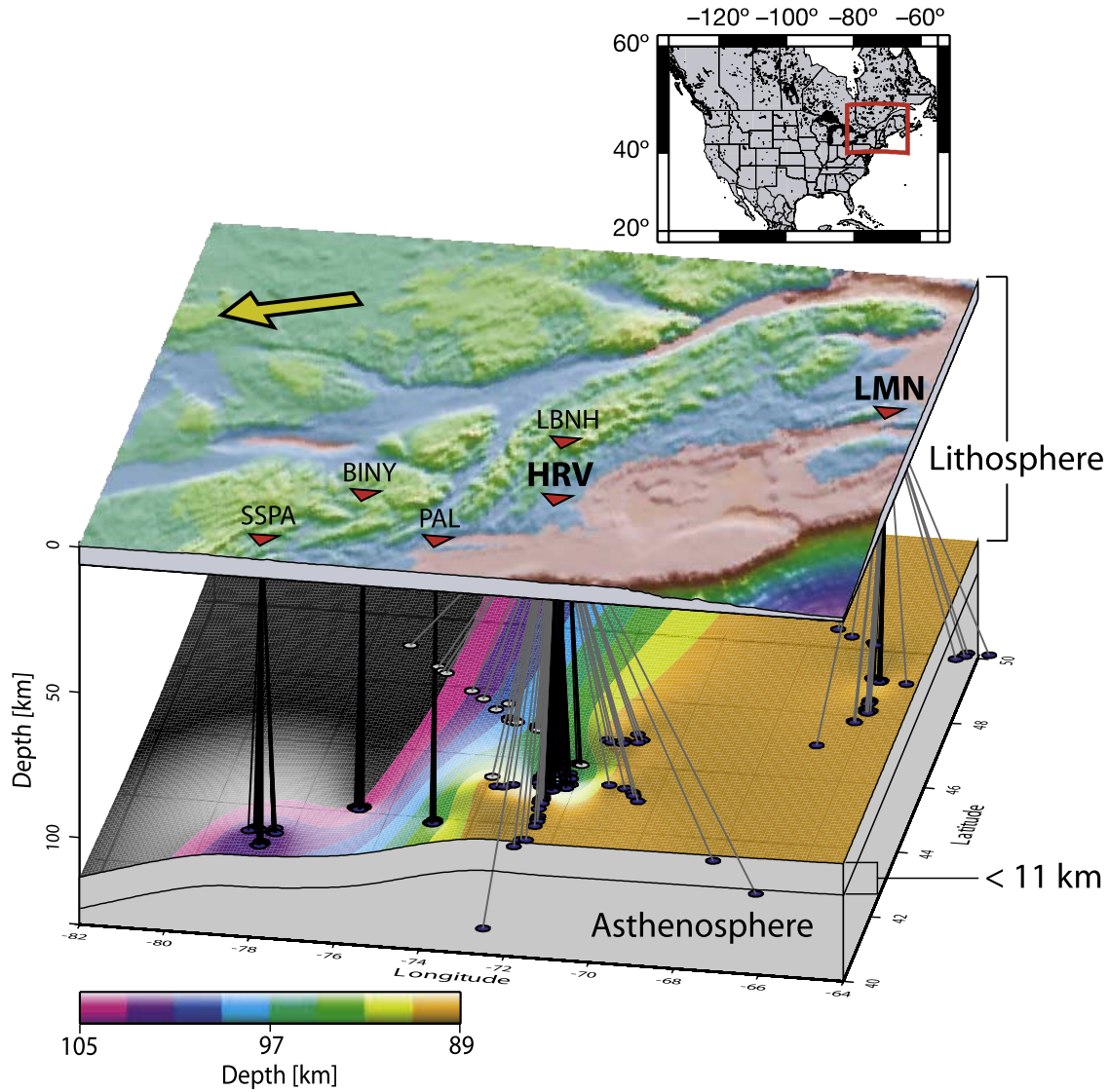
Figure 2. Three-dimensional view of the lithosphere-asthenosphere boundary and surface topography. Red box in the inset map highlights the location of the study region within North America. Shading on the top surface indicates topography. Yellow arrow points in the direction of absolute plate motion; plate velocity is 2.5 cm/yr. Red inverted triangles denote station locations. The lower surface represents the location of the base of the lithosphere interpolated from migrated *Ps* waveforms and our new migrated *Sp* waveforms recorded at stations HRV and LMN (blue circles mark conversion points). The *Sp* HRV data from northern back azimuths and the *Ps* from LBNH (grey circles mark conversion points) are not used to calculate the interpolated surface because of a discrepancy in the depth to which the phase migrates (see section 6.2). This surface ranges from 89 km (orange) to 105 km (pink) depth. Each color band covers 2 km in depth. Black lines connect *Ps* piercing points to the station at which the conversion is observed. Grey lines connect *Sp* piercing points to the station where the conversion is observed. All depths are calculated assuming $V_p/V_s = 1.8$ in subcrustal mantle.

and epicentral distances of >80°, and stacking over a wide range of distances and depths. At HRV we can use an even more conservative depth cutoff of 150 km by virtue of the larger volume of data recorded at the station. In addition, we do not use data from epicentral distances <55° since these events are incident to the discontinuity at angles beyond the critical angle for *Sp* transmission. After picking identifiable *S* phases, our deconvolved, migrated waveforms contain 56 events at HRV and 28 events at LMN (Figures 3c and 3d).

The standard deviation error bars (grey lines in Figure 3) on our deconvolved waveforms are calculated with bootstrap tests in which a random 20% of the events in the bin are randomly replaced by another random 20%, and the deconvolved, migrated waveforms are recalculated 100 times.

2.2. Imaging

[12] To image the discontinuities responsible for the *Sp* and *Ps* converted phases, the data is first transformed into its *P* and *SV* components using a free-surface transfer matrix.
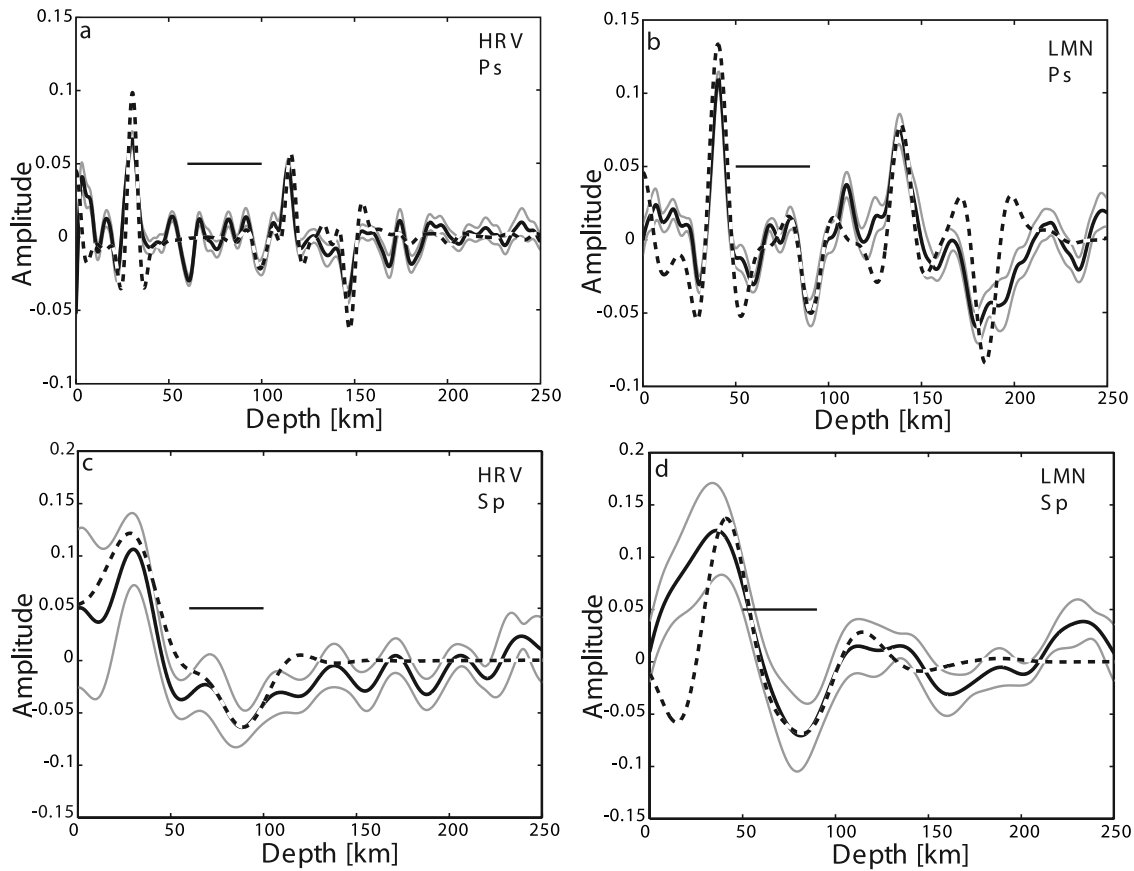
Figure 3. *Ps* and *Sp* imaging at individual stations. Black lines show data for *Ps* imaging (Figures 3a and 3b), where *P* waveforms are deconvolved from *SV* and migrated in single bins for stations HRV (Figure 3a) and LMN (Figure 3b), and *Sp* imaging (Figures 3c and 3d) where *SV* waveforms are deconvolved from *P*, migrated in single bins, and multiplied by negative one for stations HRV (Figure 3c) and LMN (Figure 3d). A positive phase corresponds to a velocity increase with depth, while a negative phase indicates a velocity decrease with depth. Error bars corresponding to two standard deviations (grey lines) were calculated with bootstrap tests in which a random 20% of the events in the bin were randomly replaced by another random 20%, and the deconvolved, migrated waveforms were recalculated 100 times. Short, horizontal, black lines plotted at amplitude 0.05 correspond to lithosphere-asthenosphere boundary depth as determined by surface wave models, defined as the greatest negative velocity gradient beneath LMN [*van der Lee*, 2002] and HRV [*Li et al.*, 2003]. Synthetic waveforms corresponding to the models obtained by inverting the data are shown for HRV and LMN (dashed lines). Crustal parameters in these models come from *Ps* inversions where phase amplitudes were not included; thus they do not match the data. Also, no discontinuities deeper than the base of the lithosphere were included in the synthetic models, so we do not expect to match phases from deeper discontinuities.

For *Sp* and *Ps* imaging each component is normalized by the maximum amplitude of its corresponding direct *S* and *P* arrival, respectively, and then weighted according to its signal-to-noise ratio. Treating *Sp* and *Ps* data separately, we perform a least squares simultaneous deconvolution in the frequency domain and migrate the resulting waveform (i.e., estimate of the Earth's impulse response) to depth using a 1-D velocity model, thus illuminating discontinuities in the Earth's shear wave structure [*Bostock*, 1998]. This process requires the application of a band-pass filter and the use of a water level, i.e., regularization, to stabilize the spectral division, two operations that in practice remove some of the signal's higher frequency content.

[13] *Sp* imaging is different than *Ps* in a few ways. We have found it necessary to enhance the signal-to-noise ratio in *Sp* imaging by applying a band-pass filter (0.01–0.175 Hz) and increasing the deconvolution water level. Fortunately, there is no risk of interference between the phase of interest and reverberations when high frequencies are eliminated in *Sp* data. Additionally, since deconvolved *Sp* phases exhibit a polarity opposite that for *Ps* imaging for a given discontinuity, we inverted the sign of *Sp* waveforms to facilitate comparisons (Figure 3).

[14] There is some variation in the character of the deconvolved *Sp* waveforms (Figures 3c and 3d) between HRV and LMN, LMN appearing slightly longer period than HRV. This difference is primarily caused by water level deviations in the spectral division associated with deconvolution. LMN data require a higher water level than HRV to reduce noise caused by the smaller number of quality events
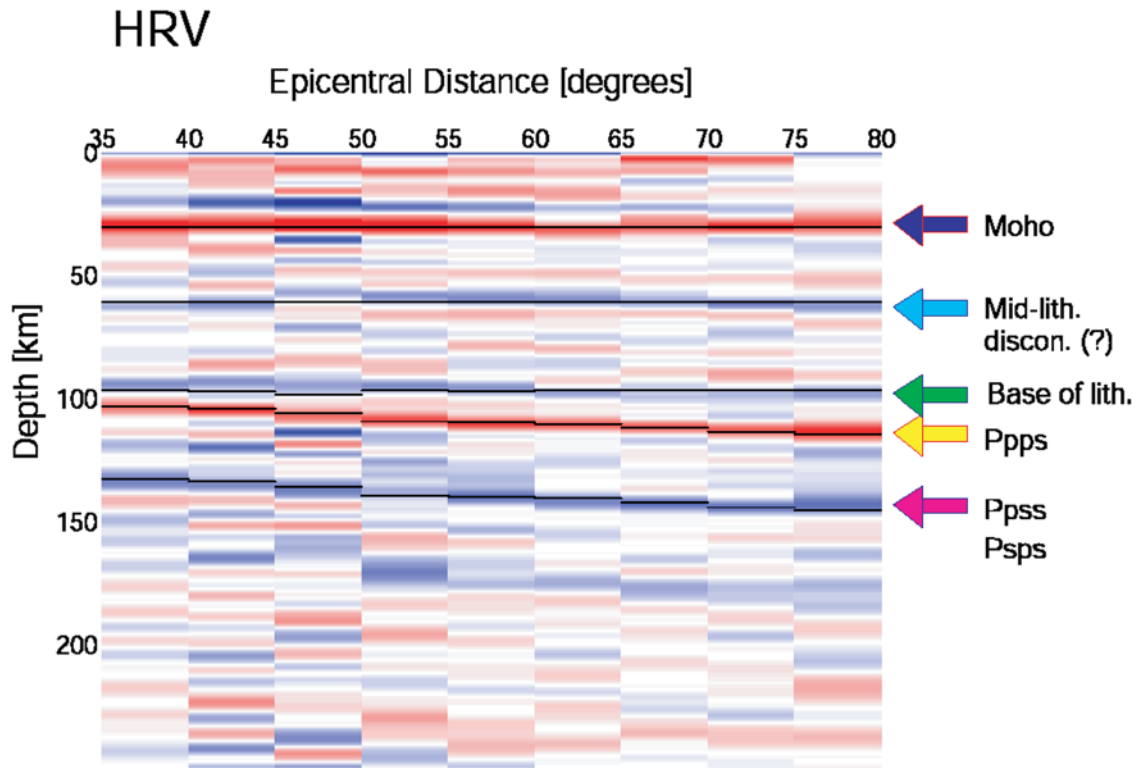
Figure 4. HRV *Ps* waveforms deconvolved and migrated in epicentral distance bins. Red signifies positive polarity, or a velocity increase with depth, while blue indicates a negative amplitude, corresponding to a velocity decrease with depth. Black lines indicate the migrated depths of synthetic phases predicted from our preferred HRV model, including direct conversions from the Moho (30 km depth), 97 km depth, and an ambiguous discontinuity at 61 km depth. Later arrivals show greater apparent depth with distance and correspond to crustal reverberations.

at LMN. However, some of the variation may be related to real earth structure.

[15] At HRV and LMN strong positive *Sp* phases associated with the Moho migrate to 30.2 km and 36 km depth, respectively (Figures 3c and 3d). At both HRV and LMN, strong negative *Sp* phases migrate to 90–99 km and 87–97 km depth, respectively, in agreement with the base of the fast lid imaged by surface wave studies [*Li et al.*, 2003; *van der Lee*, 2002], and in general agreement with the phase associated with the base of the lithosphere in our former study [*Rychert et al.*, 2005] in this region. The method for determining the range of accepted depths to the base of the lithosphere is described in more detail in sections 5.3 and 5.4. The migration model assumed to image the discontinuities in the *Sp* data includes the best fitting crustal model from inversions of *Ps* data [*Rychert et al.*, 2005] and a fixed mantle-lithospheric *S* wave velocity (4.5556 km/s) [*Musacchio et al.*, 1997]. A V_p/V_s of 1.8 is widely accepted for the shallow mantle [*Dziewonski and Anderson*, 1981; *Kennett and Engdahl*, 1991], and we employ this value in the migrated waveforms shown in this paper. However, in later sections, where we invert for the velocity gradient parameters at the lithosphere-asthenosphere boundary, we also employ values of 1.7 and 1.9 to test the sensitivity of our results to V_p/V_s.

[16] Although not the focus of this paper, deeper phases are also present in the *Sp* data. At HRV a weak positive phase with peaks at 238 km and 267 km depth is observed,

and at LMN a stronger positive phase migrates to a similar depth, 233 km. These results agree broadly with *Vinnik et al.* [2005a], who report a positive phase at somewhat shallower depths (~200 km) for stations to the west of HRV, and *Li et al.* [2002], who observe a double-pulse phase at HRV at similar depths in *Ps* data; in contrast to the *Ps* phases presented here, *Li et al.* [2002] processed their *Ps* data to emphasize energy at longer periods.

2.3. An Ambiguous 61 km Discontinuity

[17] A negative phase at 61 km depth in the *Ps* imaging at HRV suggests the existence of a discontinuity at that depth [*Rychert et al.*, 2005] (Figures 3a and 4). However, in the *Sp* image, the energy that migrates to a depth comparable to that of the 61 km discontinuity, 56 km depth, looks more like a sidelobe of the Moho (Figure 3c). Synthetic testing indicates that the amplitude of the *Sp* phase in the HRV data at 56 km is not nearly as large as would be predicted by the model derived from *Ps* data. One possible explanation for the discrepancy between the *Ps* data and *Sp* data is that the negative phase at 61 km depth in the *Ps* imaging at HRV represents a reverberation from a midcrustal discontinuity, since such a reverberation would not appear in the *Sp* data. This argument is not fully supported by the data because the direct converted phase from such a midcrustal discontinuity is not observed in either the *Ps* (Figures 3a and 4) or the *Sp* data (Figure 3c). Also, if the 61 km discontinuity were a reverberation, synthetic testing indicates that it would mi-

grate to increasing depth with respect to epicentral distance in the *Ps* imaging, i.e., ~4 km deeper at 80° epicentral distance than at 35°. Such move out is not observed in the *Ps* data (Figure 4), although such a small difference in depth between 35° and 80° may be difficult to detect. Alternatively, the 61 km discontinuity could represent a local scatterer directly beneath HRV that is sampled by *Ps*, but not by the more widely spaced *Sp* scattering points. Or, the phase could represent a change in anisotropy that is more strongly felt by *Ps* than *Sp*. However, it is important to note that the maximum effect that including the 61 km discontinuity has on the *Ps* models for the gradient at the lithosphere-asthenosphere boundary is small, a decrease in the magnitude of the required contrast that is <1% [*Rychert et al.*, 2005]. Therefore, since the 61 km discontinuity is not observed in *Sp* imaging and its effects on the inversion for the lithosphere-asthenosphere boundary are secondary, we do not to include it at HRV in either the *Ps* or the *Sp* modeling presented here.

3. S_p and P_s Sensitivities

[18] Before proceeding with the inversion of the observed waveforms, we first explore the sensitivity of *Ps* and *Sp* phases to various aspects of the modeled structures. We divide this exploration into five sections: in section 3.1 we discuss the effects of individual parameters including absolute depth, V_p/V_s, impedance contrast, gradient thickness, and dominant period on the character of converted phases; in sections 3.2 and 3.3 we discuss the sensitivity of *Ps* and *Sp* phases to velocity gradients of various thicknesses; in section 3.4 we discuss the importance of impedance contrast parameters (V_p, V_s, and density); and in section 3.5 we discuss a caveat regarding discontinuity topography.

3.1. Effects of Parameters: Depth, V_p/V_s, Impedance, Gradient Thickness, and Dominant Period

[19] Waveforms converted at a discontinuity are influenced by five main parameters: the impedance contrast at the discontinuity, the depth range over which the velocity contrast occurs, the absolute depth of the discontinuity, V_p/V_s in the layers shallower than the discontinuity, and the dominant period of the incident waveform (Figure 5a). To attain a more intuitive sense for how these parameters affect the character of the converted phase, we compare the character of converted phases in deconvolved, migrated synthetics for variations in a single parameter (Figure 5).

[20] First, depth affects exclusively the timing of the phase (not illustrated in Figure 5). Increasing the depth of a discontinuity results in a converted phase that migrates to greater depth. The peak of the converted phases corresponds to roughly the midpoint of the velocity gradient in depth for linear gradients, or the midpoint of the sharpest contrast for exponential gradients. Similarly, the timing of the phases depends on V_p/V_s in the layers shallower than the depth of the converted phase (not illustrated in Figure 5). This is the primary effect of V_p/V_s, and the individual effects of *P* wave and *S* wave velocities are described in more detail in section 3.4.

[21] Third, increasing the impedance contrast at a boundary creates *Sp* and *Ps* phases with larger amplitudes. Here we present a change in shear wave velocity to demonstrate

the effect of impedance contrast (Figure 5b) since we will demonstrate in section 3.4 that shear wave velocity contrast is the most influential component of impedance contrast.

[22] Fourth, increasing the depth range, i.e., gradient thickness, over which the discontinuity occurs creates a broader phase with decreased amplitude (Figure 5c). This effect is muted in *Sp* imaging mainly because *Sp* is an inherently longer period wave, and thus less sensitive to the depth range over which gradients occur.

[23] Fifth, increasing the dominant period of the incident waveform results in a broader phase and possible increase in amplitude (Figure 5d). Though not illustrated in Figure 5, note that changing the dominant period of incident *Ps* and *Sp* waveforms has no effect on the amplitude of conversions from a step function shaped discontinuity. The asymmetrical behavior of long-period *Ps* phases on the left side of Figure 5d is related to interference with remnants of the incident *P* phase left over on the *S* wave component due to imperfect phase decomposition.

3.2. Rule of Thumb Sensitivity to Gradient Thickness

[24] The sensitivity of seismic waves to gradient thickness was initially demonstrated using $P'P'$ precursors (period equals 1 s) from a discontinuity at 650 km depth which required a gradient that occurred over 4 km or less to attain 2.5% of the amplitude of the incident phase [*Richards*, 1972]. We now assess the validity of the general rule of thumb which states that converted phases are sensitive to gradients that occur over depth ranges of up to wavelength/ 2 [e.g., *Bostock*, 1999]. We consider *Ps* and *Sp* phases converted in a model where a 5% velocity drop is divided into two step function velocity discontinuities that occur at a variable depth range from each other (Figure 6); *S* wave velocity = 4.556 km/s in the upper layer and $V_p/V_s = 1.8$ and density = 3.32 g/cm^3 in both layers.

[25] We observe constructive interference between the synthetic phases until the separation distance reaches roughly 7 km and 28 km for *Ps* and *Sp*, respectively. The deconvolved waveforms corresponding to these synthetics are indicated by the dashed lines in Figures 6b and 6c. However, there is a range of thicknesses where the phases pull-apart in the deconvolved waveforms, 7–8 km and 28– 36 km. These values correspond to average wavelength-to-gradient thickness ratios of roughly 2 for both *Ps* and *Sp*, where the average wavelength corresponds to the average value from the layers on either side of the velocity discontinuity. Note that when multiple layers are implemented to construct a smoother version of the same velocity gradient, as done in our inversions, converted phases that were split into two in this test maintain their shape as singular phases with larger amplitudes until greater gradient thicknesses. However, for the case where a discontinuity is composed of two step function drops, the waveforms are indeed sensitive to a depth separation of wavelength/2.

3.3. Parameterized Sensitivity to Gradient Thickness

[26] While the tests in sections 3.1 and 3.2 address the effects of individual parameter values, globally waves encounter a wide range of discontinuity parameters. To achieve a more quantitative description of waveform sensitivity, we compare the amplitude of synthetic *Ps* and *Sp* phases of various dominant periods converted at gradational
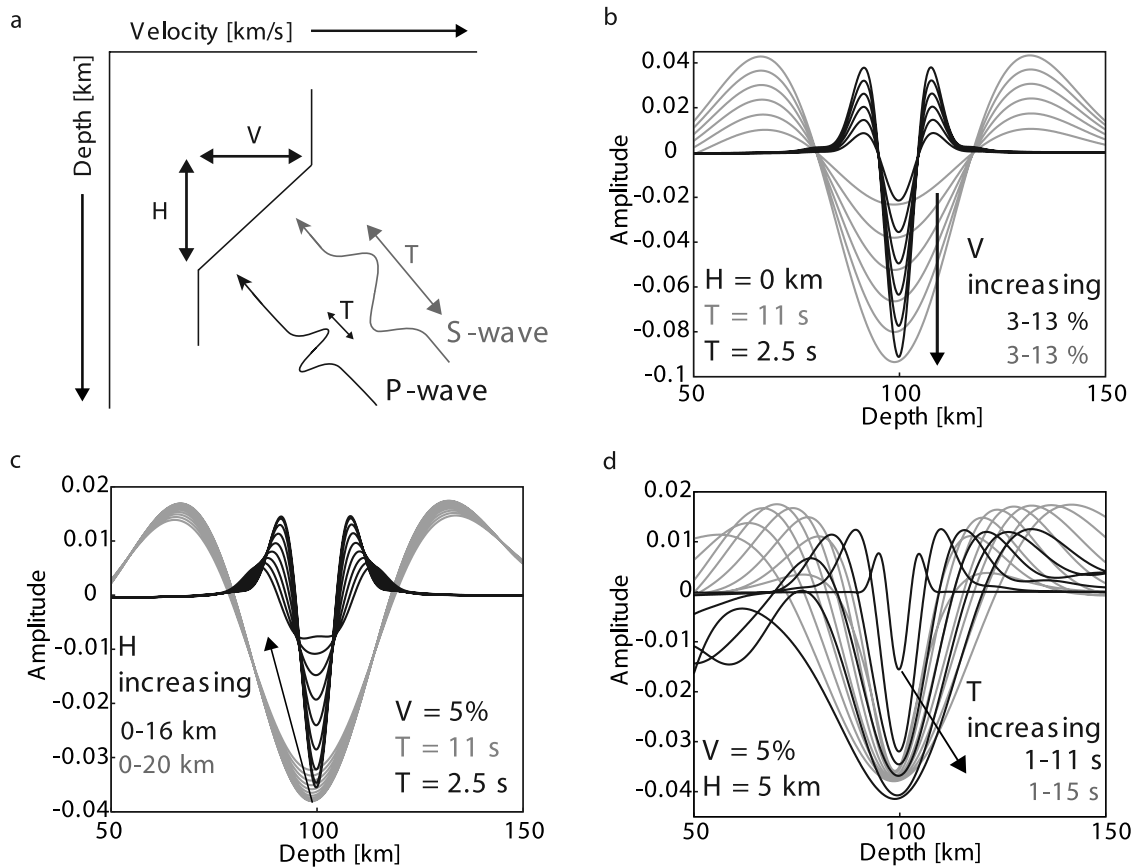
Figure 5. Effects of a single parameter on the character of a conversion. Deconvolved and migrated *Ps* (black lines) and *Sp* (grey lines) synthetic waveforms are shown for models with variations in a single parameter. (a) Schematic of the parameters that are varied in Figures 5b, 5c, and 5d, including the magnitude of the velocity gradient (V), thickness of the velocity gradient (H), and the dominant period of the incident waveform (T). (b) Effect of variations in the magnitude of the velocity drop. The dominant period of the incident *S* wave is held at 11 s, and that of the *P* wave is held at 2.5 s. The thickness of the gradient is held at 0 km (a single step function). As the shear wave velocity contrast increases from 3 to 13% in increments of 2%, the amplitudes of both the converted *Ps* and *Sp* phases increase uniformly. (c) Effect of variations in the thickness of the velocity gradient. The magnitude of the velocity drop is held at 5%, and the dominant periods of the incident waveforms are held at the same values as in Figure 5b. As the thickness varies from 0 to 16 km in increments of 2 km, the *Ps* phase loses amplitude and broadens. The effect of variations in gradient thicknesses (0 to 20 km in increments of 2 km) on the character of *Sp* phases is much more muted. (d) Effect of variations in the dominant period of the incident waveform. Velocity drop is fixed at 5%, and gradient thickness is fixed at 5 km. As the dominant period of the incident *P* wave increases from 1 to 11 s in increments of 2 s, the *Ps* phase broadens and increases in amplitude. As the dominant period of the incident *S* wave increases from 1 to 15 s in increments of 2 s, the *Sp* phase broadens, but amplitude effect are more muted. The asymmetrical behavior of long-period *Ps* phases on the left side of Figure 5d is related to interference with remnants of the incident *P* phase left on the *S* wave signal.

and sharp discontinuities (Figure 7). The model assumes a 6% velocity contrast in *P* and *S* wave velocity. V_s in the upper layer and density and V_p/V_s in both layers are identical to those of section 3.2. We consider amplitudes of the transformed *S* wave component for *Ps* conversions and the transformed *P* wave component for *Sp* conversions. We present our results in terms of both the average wavelength across the boundary (solid lines in Figure 7) and the incident wavelength (dashed lines in Figure 7). Note that the raw (undeconvolved) amplitudes of both *Ps* and *Sp* phases are significantly reduced when the average wavelength to gradient thickness ratio reaches 2, the case

most analogous to the rule of thumb explored in section 3.2 (with deconvolved waveforms). Also, note that the greatest difference in sensitivity between *Sp* and *Ps* phases lies in the inherently greater dominant periods and wavelengths of *Sp* phases compared to *Ps* phases.

3.4. Sensitivity to Impedance Parameters: Density, *P* Wave and *S* Wave Velocities

[27] To determine what aspect of impedance contrast most affects *Ps* and *Sp* phases we test the sensitivity of *Ps* and *Sp* waves to *S* wave and *P* wave velocity and density in the lithosphere and the asthenosphere. We present transmis-

sion coefficients [*Aki and Richards*, 1980] to describe the sensitivities of *Ps* and *Sp* waves to density, *P* wave velocity, and *S* wave velocity (Figure 8). In this case we have not multiplied *Sp* amplitudes by negative one to agree with *Ps* amplitudes, so *Ps* amplitudes are negative and *Sp* amplitudes are positive for a conversion due to a velocity drop with depth.

[28] *S* wave velocity contrasts dominate the transmission coefficients. For *Ps*, the effects of *S* wave velocity contrasts are at least 30 times that of similar *P* wave velocity contrasts (Figures 8e and 8f). Moreover, there is no *Ps* conversion due to a *P* wave velocity drop when no other contrast (density or *S* wave velocity) exists (Figure 8b) [*Bank and*

Bostock, 2003]. For *Sp*, again the effect of *P* wave velocity is negligible, except for smaller epicentral distances (<70°) (Figure 8k), which would have little effect on our deconvolved waveforms, since our data is from a wide epicentral distance range.

[29] Density also has a minimal effect on the amplitude of converted phases. For *Ps*, the effects of *S* wave velocity contrasts are up to 20 to 40 times larger than those caused by similar density variations (Figures 8c and 8f versus Figures 8a and 8d). For *Sp*, the effects of density are negligible or nonexistent except for small epicentral distances (<70°) when no *S* wave velocity drop is presupposed (Figure 8g). Again, this effect would not be visible in our results since we accept a wide epicentral distance range. In the end, the parameter that dominates the amplitude of *Ps* and *Sp* conversions is the shear wave velocity contrast at the boundary.

3.5. Topography

[30] Topography on a discontinuity can locally focus or defocus the wavefield, affecting the inferred location and properties of velocity gradients [e.g., *van der Lee et al.*, 1994]. We do not model topography effects in our waveforms, but because the depth to the lithosphere-asthenosphere boundary appears to vary relatively gradually between stations (Figure 2), this choice likely does not introduce significant bias into our results. Moreover, it has been shown that the overall effect of topographic structure on stacks of converted phases is typically a reduction in phase amplitude since a primary effect of boundary topography is a variation in the depth to which conversions migrate [*van der Lee et al.*, 1994]. Therefore the velocity drops inferred from our modeling likely represent conservative estimates.

4. Inversion Methods

[31] Damped least squares inversions are performed separately for *Ps* and *Sp* using the migrated waveforms from our best stations, HRV and LMN, to determine the gradient
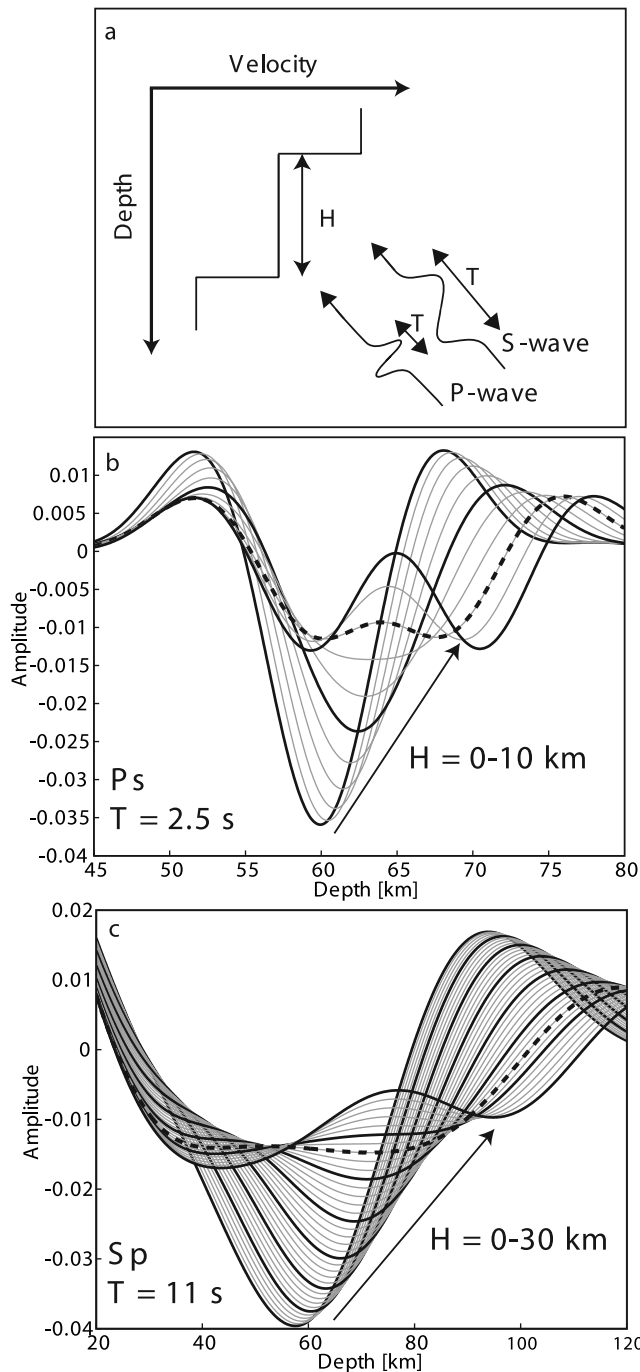

Figure 6. Rule of thumb, wavelength/2 sensitivity. Deconvolved, migrated *Ps* and *Sp* synthetic waveforms are shown for a velocity drop that is divided into two step function-like discontinuities. (a) Schematic of the parameters, which include the distance between the discontinuities (H) and two different dominant periods (T). T is set at representative values for *Ps* (2.5 s) and *Sp* (11 s). The distance (depth range) between the discontinuities is increased in increments of 1 km from (b) 0 to 10 km (*Ps*) and from (c) 0 to 30 km (*Sp*). The bold dashed line indicates the distance at which the single coherent phase breaks into two phases, at a gradient thickness of approximately (average wavelength)/2. Though not shown here, the same break is independently observed in the raw synthetic waveforms at the same depth separation (H) as seen in the deconvolved migrated waveforms, 8 and 28 km for *Ps* and *Sp* phases, respectively. The model includes a 5% velocity drop, an *S* wave velocity in the upper layer of 4.5556 km/s, density of 3.32 g/cm^3, and $V_p/V_s = 1.8$. The slownesses are set at representative values of 8.019 and 11.897 s/deg for *Ps* and *Sp*, respectively.
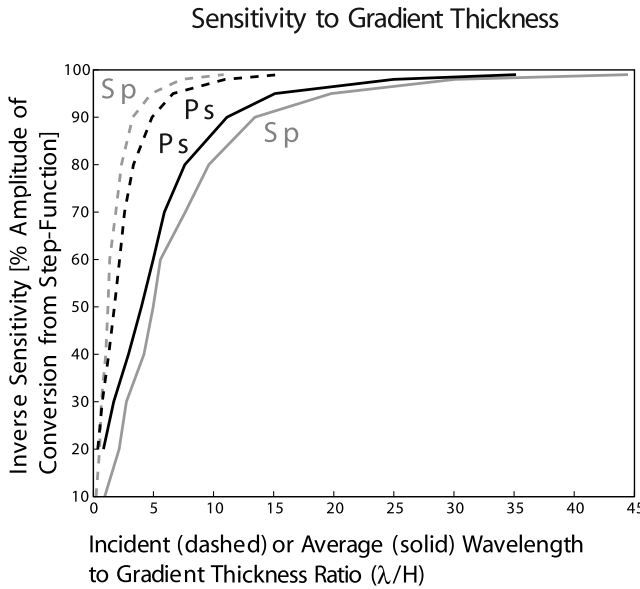
Sensitivity to Gradient Thickness

Figure 7. Sensitivity of *Ps* and *Sp* to velocity gradient thickness. The amplitudes of converted *Ps* (black lines) and *Sp* (grey lines) phases from velocity gradients of various thicknesses are compared to those from single step function velocity drops of the same magnitude. We consider the amplitudes of synthetic seismograms on the transformed *S* component for *Ps* conversions and the transformed *P* component for *Sp* conversion. Since sensitivity is dependent on the dominant period of the incident waveform, we have also varied this parameter. Sensitivity to a given gradient can then be described as the percent amplitude of a converted phase from a step function velocity drop exhibited by a conversion with a given incident (dashed line) or average (solid lines) wavelength-to-gradient thickness ratio. Our model assumes a 6% velocity drop in *P* and *S* wave velocity, *S* wave velocity in the upper layer of 4.556, density of 3.32 g/cm^3 and V_p/V_s = 1.8. The slownesses are set at representative values of 6.34 and 12.12 s/deg for *Ps* and *Sp*, respectively.

of the velocity contrast at the base of the lithosphere. Predicted waveforms and partial derivatives are recalculated for each iteration. The synthetic seismograms used to determine partial derivatives are calculated using a propagator matrix method [*Keith and Crampin*, 1977]. Throughout all of the inversions, the number of layers in depth is fixed to minimize the number of assumptions regarding crust and mantle structures. At both HRV and LMN the layers include a crust, mantle-lithosphere, and asthenosphere based on the observed converted phases in the *Sp* data. The boundary between the lithosphere and the asthenosphere is characterized by both a step function velocity drop and a velocity gradient of variable thickness. Note that in our assumptions concerning layering we do not include the previously discussed ambiguous discontinuity at 61 km at HRV (see section 2.3).

4.1. Crustal Inversion

[32] We first invert for crustal thickness and average crustal V_p and V_s at each station (HRV and LMN) using the timing of the *Ps* phase from the Moho and the timing of

its two first-order reverberations in nine epicentral bins (Table 1 and Figure 4) [*Rychert et al.*, 2005]. Note that this method of determining crustal properties differs from other widely employed approaches [*Ammon et al.*, 1990; *Zhu and Kanamori*, 2000]. *Zhu and Kanamori* [2000] determine crustal thickness and V_p/V_s by maximizing the amplitudes of stacked Moho conversions and their first-order reverberations. *Ammon et al.* [1990] directly invert *Ps* waveforms for multilayer crustal models.

[33] In our crustal modeling we use the timing of *Ps* instead of *Sp* because *Ps* has a clear first arrival and clear reverberations from the Moho which may be used as independent information, providing excellent resolution of crustal parameters. Assuming a single-layer crust allows us to minimize assumptions regarding structure internal to the crust. However, a single-layer crustal model also oversimplifies real crustal structure, and the magnitude of the velocity increase at the Moho is almost certainly smaller than the values implied by these crustal velocities. Therefore we do not attempt to match the amplitude of Moho conversions in our inversions, and we evaluate the impact that assuming a single-layer crust has on the inferred properties of the lithosphere-asthenosphere boundary. We find that the maximum effect that gradational crustal velocities can have on the magnitude of the velocity drop at the lithosphere-asthenosphere boundary required by our inversions is <0.5% and <1% for *Ps* and *Sp* inversions, respectively. We calculate the errors in our crustal parameters using the formal 95% confidence limits from the inversion.

4.2. Lithosphere-Asthenosphere Boundary Inversion

[34] We invert the complete waveform shape of the converted *Ps* and *Sp* phases from the lithosphere-asthenosphere boundary separately to determine the properties of the associated velocity gradient. The waveforms are inverted separately to achieve a better understanding of the different sensitivities of the two types of converted phases. We invert for the dominant period of the incident wave, the shear wave velocity drop, and the absolute depth to the velocity contrast assuming a linear velocity gradient. Density, gradient thickness, and V_p/V_s values are held fixed in each inversion. However, the inversions are performed assuming four to five different gradient thicknesses, and even though gradient parameters (magnitude and thickness) are relatively insensitive to *P* wave velocity (see section 3.4), we also vary lithospheric and asthenospheric V_p/V_s. A V_p/V_s of 1.8 is a commonly assumed value for the shallow mantle [*Dziewonski and Anderson*, 1981; *Kennett and Engdahl*, 1991], but we also employ a low-end value, 1.7, for demonstrative purposes (Table 1). A minimum mantle V_p/V_s of 1.7 is suggested by xenolith data [*Lee*, 2003]. In some cases V_p/V_s is fixed at a constant value (1.7 or 1.8) in the lithosphere and the asthenosphere, and in others it linearly increases or decrease between these values over the boundary. We also present the case in which V_p/V_s varies from 1.8 in the lithosphere to 1.9 in the asthenosphere. This example explores how higher V_p/V_s values that might be created by partial melting in the asthenosphere [*Hammond and Humphreys*, 2000; *Karato*, 2003] would affect our results. We do not vary density since it does not significantly impact our results (section 3.4). Holding a number of parameters fixed while others vary is necessary for the
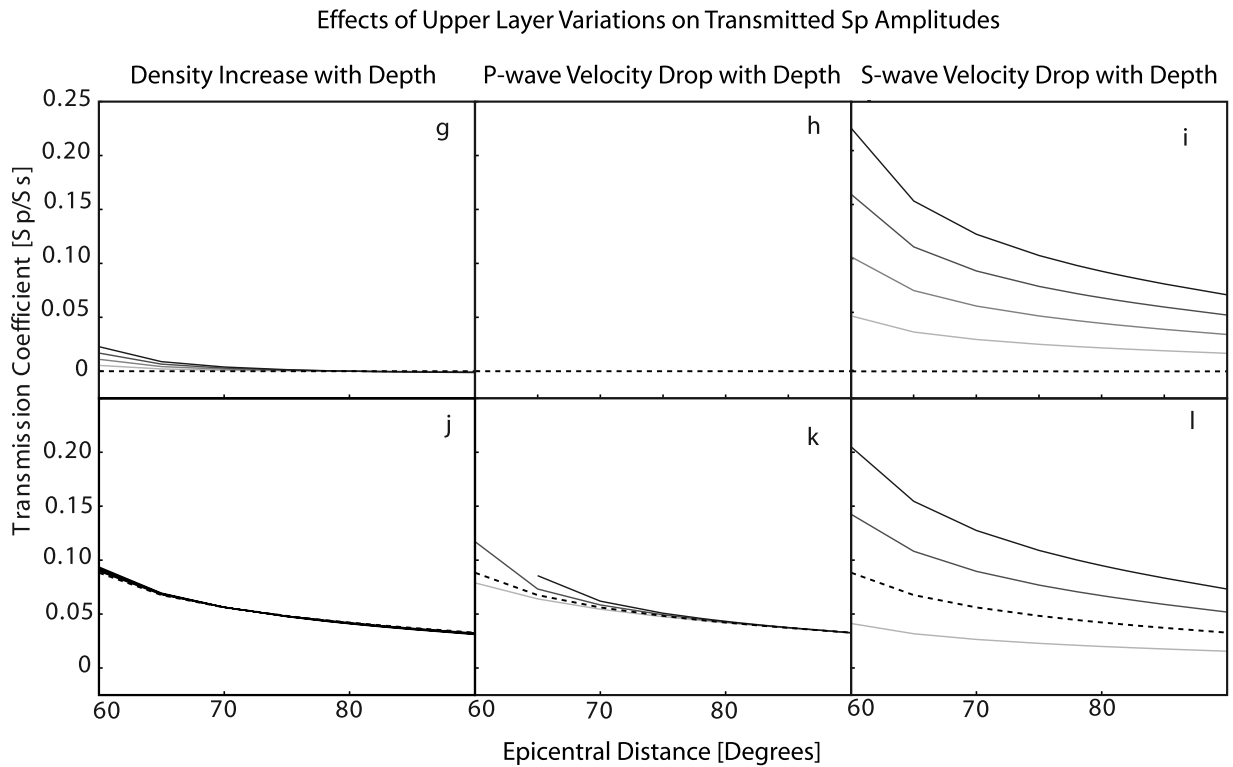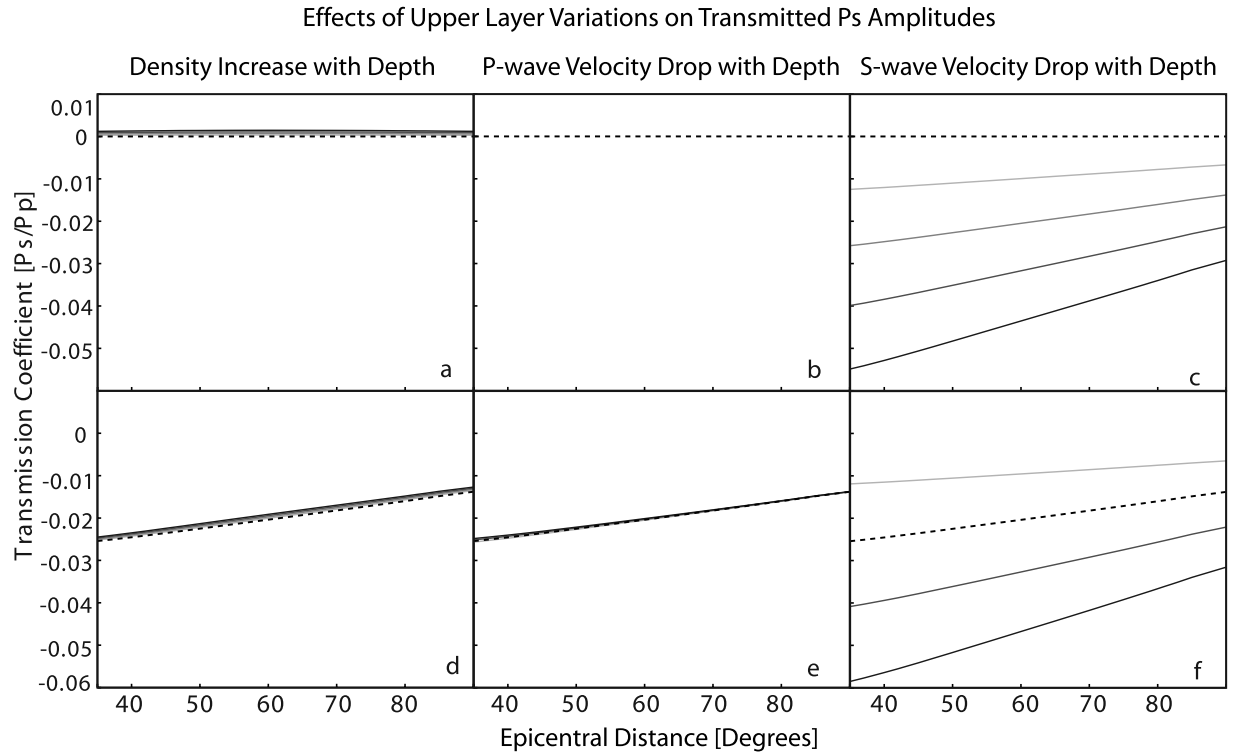
Effects of Upper Layer Variations on Transmitted Ps Amplitudes

Figure 8

stability of our inversions, but grid searches confirm that no other models exist with better fits than those of our final results.

[35] A variety of tests including forward modeling, grid searches, and formal inversions indicate strong trade-offs between the parameters, especially for the case of *Ps*

(section 3.1). In our former inversions of *Ps* data alone we constrained the dominant period of the incident *P* wave independently, and in turn limited the possible variation in the other parameters [*Rychert et al.*, 2005]. However, here we use the independent information from both *Ps* and *Sp* inversions to constrain the acceptable gradient parameters.

Table 1. Inversion Summary

Inversion	Data	Model Parameter for Which We Inverted	Parameters Held Fixed
Step 1, crust[a]	timing of the Moho and the first two reverberations in nine *Ps* epicentral bins	crustal thickness, crustal V_s, crustal V_p	crustal density
Step 2, lithosphere-asthenosphere boundary	deconvolved and migrated converted *Ps* and *Sp* waveforms from the base of the lithosphere	asthenospheric V_s, period of incident wave, depth to discontinuity	parameters related to the crust (from step 1), density of lithosphere and asthenosphere, thickness of velocity gradient,[b] V_p/V_s of lithosphere and the asthenosphere[b]

[a]In step 1, the amplitude of the Moho and reverberations are not considered. The crust is assumed to be a single layer with an average velocity, thereby simplifying structure and minimizing assumptions.

[b]Inversion has been performed for various values (four to five thicknesses and two to three V_p/V_s values) of parameters to determine the effects of these parameters on the final results.

We accept the overlapping error bar space of the *Ps* and *Sp* inversions (see sections 5.1 and 5.2).

4.3. Normalization

[36] Care is taken to accurately calculate predicted migrated waveform amplitudes and the partial derivatives of the predicted migrated waveforms with respect to discontinuity parameters. First, the crustal parameters in the model used to calculate synthetics are fixed at the values determined by *Ps* inversions (Tables 1 and 2). Second, synthetics are calculated for the *S* slowness of each of the *Sp* data waveforms, and the *P* slowness of each of the *Ps* data waveforms. Finally, the synthetics are scaled to the amplitudes of their normalized, real waveform counterparts, and processed with water levels and filters identical to those applied to the real data (section 2.2). This procedure ensures that we accurately account for differences in phase amplitude produced by waveforms with varying *P* wave and *S* wave incidence angle.

4.4. Migration Model

[37] When matching deconvolved, migrated waveforms in depth, it is important that the migration model not bias the results. Therefore we require the migration model to match our best fitting model. To accomplish this, the parameters that we hold fixed in the inversions for the gradient at the lithosphere-asthenosphere boundary are held fixed at identical values in the migration model (Table 1). The parameters that vary during the inversion that are related to earth structure (i.e., the depth to the discontinuity and shear wave velocity contrast, but not the dominant

period of the incident waveform) are updated in the migration model once several iterations are completed and convergence is achieved. Then the data are reprocessed using the new migration model, and the iterative inversion is rerun. The process is repeated until subsequent inversions no longer yield perturbations to the best fitting model, and the migration model is a perfect match to the best fitting model. The number of layers in the migration model remains constant throughout all steps of the inversion.

4.5. Gradient Shape

[38] All inversions reported here assume a linear velocity gradient at the lithosphere-asthenosphere boundary. However, we experimented with both *Ps* and *Sp* conversions at exponential gradients. For linear and exponential gradients that occur over the same depth range, the magnitude of the velocity contrasts required to fit our data are nearly identical regardless of shape. Additionally, the depth of the sharpest part of the exponential corresponds to the peak of the deconvolved, migrated converted phase. Our final results are not significantly influenced by the shape of the velocity gradient.

5. Results
5.1. Gradient Characteristics: Magnitude and Depth Extent of the Velocity Drop

[39] The inversion results demonstrate the different sensitivities of *Ps* and *Sp*. We find that *Sp* phases predict similar velocity drops, all within 2% of each other for a given station, and all within 1% of each other for a given station

Figure 8. Sensitivity of *Ps* and *Sp* to *S* wave velocity, *P* wave velocity, and density. Variations in the *Ps* (Figures 8a–8f) and *Sp* (Figures 8g–8l) transmission coefficients are shown for 3, 6, 9, and 12% contrasts (respectively indicated by increasing line darkness) in the three parameters: density, *P* wave velocity, and *S* wave velocity. Thick, dashed, black line corresponds to the transmission coefficients for the respective reference model. In Figures 8a–8c and 8g–8i, reference values in the upper (lithosphere) and lower (asthenosphere) layers are density of 3.32 g/cm^3, *P* wave velocity of 8.2 km/s, and *S* wave velocity of 4.556 km/s. Only one upper layer parameter is varied at a time; density is decreased in Figures 8a and 8g, *P* wave velocity is increased in Figures 8b and 8h and *S* wave velocity is increased in Figures 8c and 8i. In Figures 8d–8f and 8j–8l, a 6% *S* wave and/or *P* wave velocity contrast and a 0% density contrast is assumed as a reference model; in other words, the reference values described for Figures 8a–8c and 8g–8i are assumed in the asthenosphere, a 6% drop in *S* wave velocity with depth is assumed when upper layer *P* wave velocity varies to give 3–12% drops with depth in Figures 8e and 8k, a 6% drop in *P* wave velocity with depth is assumed as upper layer *S* wave velocity varies to give 3–12% drops with depth in Figures 8f and 8l, and a 6% velocity drop with depth is assumed in both *P* wave and *S* wave velocity as upper layer density decreases in Figures 8d and 8j. *Sp* amplitudes are only plotted for events from distances of 60° and greater since the critical angle for *Sp* transmission is reached for most examples at 55°, and for the case with a 12% velocity contrast (Figure 8k) at 60°.

Table 2. Inversion Results

| | | Lithosphere Ps | | Lithosphere Sp | | | Lithosphere-Asthenosphere |
Parameter	Crust	$V_p/V_s = 1.8$	$V_p/V_s = 1.7$	$V_p/V_s = 1.8$	$V_p/V_s = 1.7$	Parameter	Boundary
				Station HRV			
V_p/V_s	1.68 ± 0.01[a]	1.8[b]	1.7[b]	1.8[b]	1.7[b]	V_p/V_s	$1.7-1.8$[b]
Maximum depth, km	30.2 ± 0.3[a]	99 ± 0.1[a]	104.6 ± 0.1[a]	$89.5-90.4$[a]	$95.8-98.5$[a]	gradient thickness	$5-6$ km[b]
V_s, km/s	3.79 ± 0.05[a]	4.556	4.556	4.556	4.556	velocity drop	$5.3-7.4\%$[a]
				Station LMN			
V_p/V_s	1.75 ± 0.04[a]	1.8[b]	1.7[b]	1.8[b]	1.7[b]	V_p/V_s	$1.7-1.8$[b]
Maximum depth, km	41 ± 2[a]	91 ± 0.3[a]	95 ± 0.3[a]	$86.6-89.5$[a]	$92.1-96.5$[a]	gradient thickness	11 km or less[b]
V_s, km/s	3.7 ± 0.9[a]	4.556	4.556	4.556	4.556	velocity drop	$6.0-9.6\%$[a]

[a]Parameter for which we inverted.
[b]Inversions were performed for several values of these parameters to determine their effects on the final results.

and V_p/V_s assumption (Figure 9). However, the short-period nature of *Ps* phases creates a strong sensitivity to gradient thickness, and the phases predict increased velocity drops for larger gradient thicknesses. The intersection of the 95% confidence limits for the separate *Ps* and *Sp* inversions were used to define the parameter space that jointly fits the data (Figure 9 and sections 5.2 and 5.4).

[40] Accepting all models within the intersection of the 95% confidence limits for either V_p/V_s (1.7 or 1.8) results in a 5.3–7.4% velocity contrast the occurs over 5–6 km at
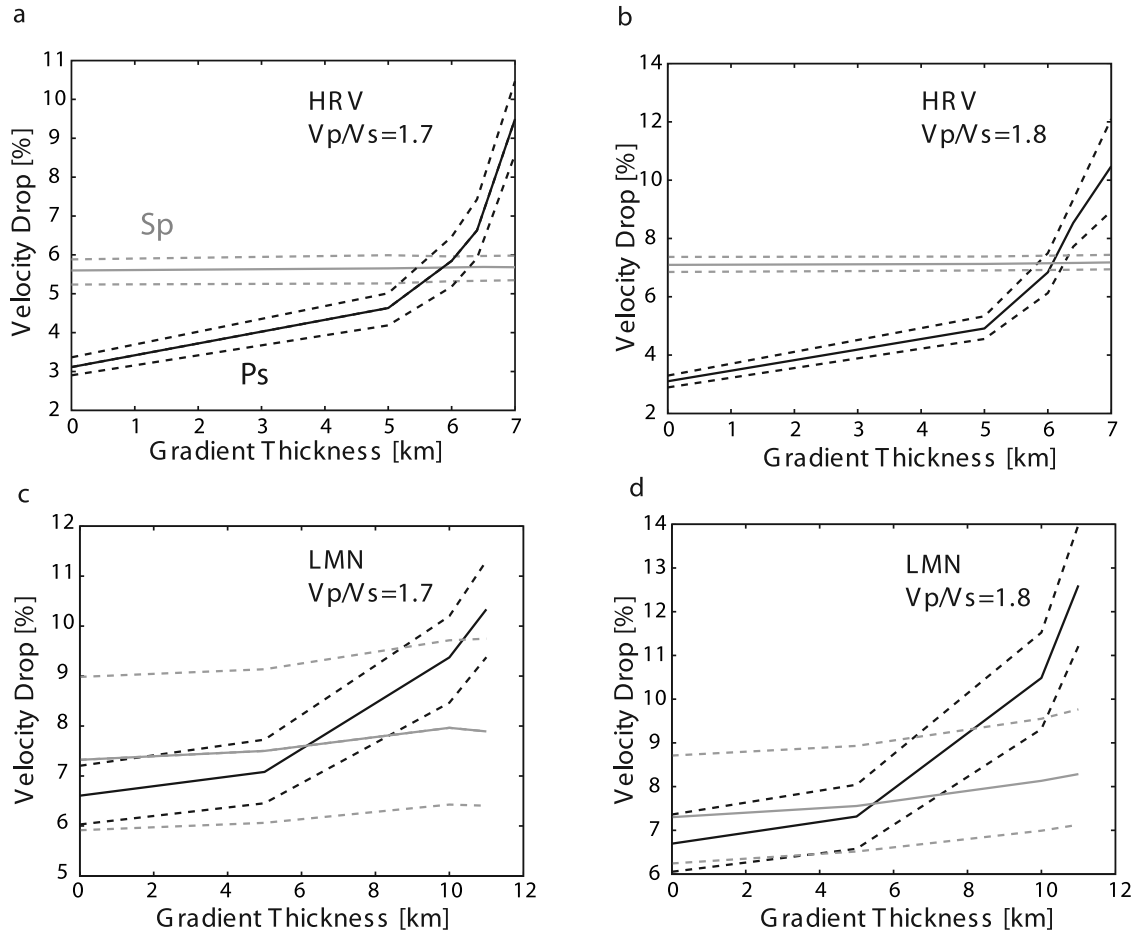

Figure 9. Inversion results for gradient characteristics. The best fitting models from *Ps* (black lines) and *Sp* (grey lines) inversions are shown. 95% confidence limits (dashed lines) were determined by performing a grid search in velocity, setting all other parameters fixed, and then performing an *F* test (section 5.4 and Figure 12). The confidence limits correspond to the intersection points of the 95% confidence limit lines with the corresponding residual curve in Figure 12. (a) Best fitting results at HRV assuming $V_p/V_s = 1.7$ in the subcrustal lithosphere and the asthenosphere, (b) HRV, $V_p/V_s = 1.8$, (c) LMN, $V_p/V_s = 1.7$, and (d) LMN, $V_p/V_s = 1.8$.
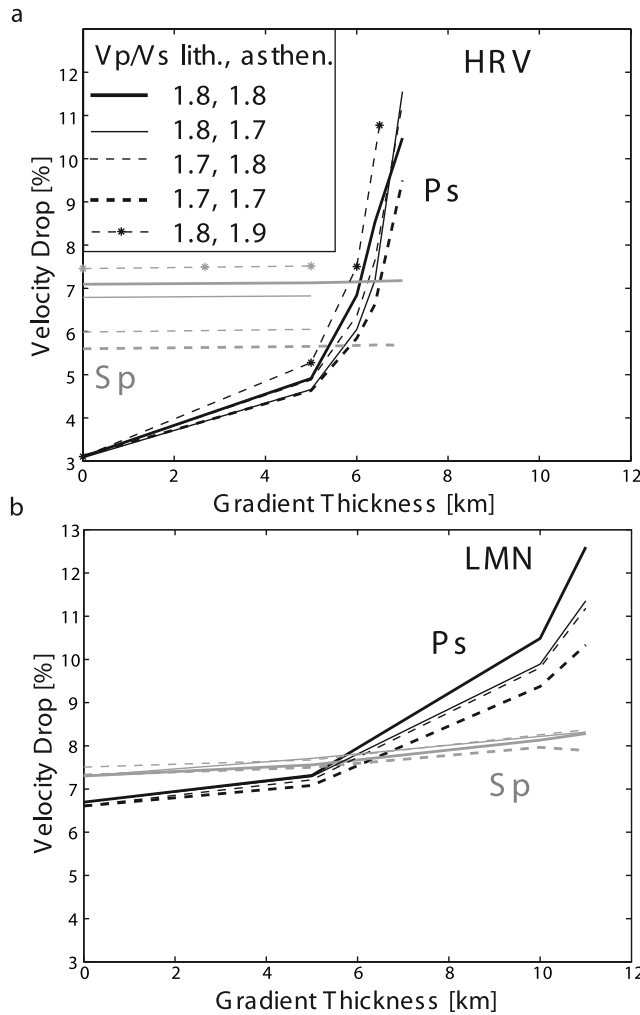
a

b

Figure 10. Expanded inversion results for gradient characteristics. All best fitting Sp models (grey lines) versus Ps model (black lines) are shown for (a) HRV and (b) LMN. Thick lines indicate models where V_p/V_s remains constant at 1.8 (solid) or 1.7 (dashed) over the lithosphere-asthenosphere boundary. Thin lines indicate models where V_p/V_s drops from 1.8 to 1.7 (solid), rises from 1.7 to 1.8 (dashed), or rises from 1.8 to 1.9 (dashed with stars) with increasing depth over the lithosphere-asthenosphere boundary.

HRV, and a 6.0–9.6% velocity contrast that occurs over 11 km or less at LMN (Table 2). Acceptable gradient parameter ranges for models in which V_p/V_s varies over the gradient thickness from 1.7 to 1.8 or vice versa are in general agreement with those in which V_p/V_s is held constant at similar values across the boundary (Figure 10), allowing us to focus on models with a fixed V_p/V_s value (Figure 9), and once again demonstrating the insignificance of V_p in determining velocity contrast and gradient thickness (section 3.4).

[41] Increasing V_p/V_s in the asthenosphere to even higher values, as might be expected for partial melting in the asthenosphere [Hammond and Humphreys, 2000; Karato, 2003] still has a relatively minimal effect on our results. However, it is worth noting that such an increase only sharpens our required shear wave velocity gradient. In the case of an asthenospheric V_p/V_s of 1.9 (Figure 10a), the required velocity gradient must be ~0.4% greater and

~0.1 km thinner than the case of constant $V_p/V_s = 1.8$, near the region of intersecting Ps and Sp models at HRV. For simplicity, we focus on results using $V_p/V_s = 1.7$ and $V_p/V_s = 1.8$ throughout the rest of the paper. Overall, although V_p/V_s has some influence on the gradient parameters in our models, we find that its effect is relatively small relative to the magnitude of our best fitting shear wave velocity drops. In most cases V_p/V_s effects are completely within our error bars for shear wave velocity drop.

5.2. Caution Interpreting P_s and S_p Inversions Together: Frequency-Dependent Velocity Gradients

[42] At first glance, the intersection of the parameter space for best fitting Ps and Sp models may seem like the solution of our inversions. However, since Ps and Sp waves exhibit different dominant periods, and attenuation is frequency-dependent, it is possible that the solution could correspond to one parameter space for Ps and another for Sp if a significant fraction of the observed velocity drop is caused by increased attenuation in the asthenosphere.

[43] In order to assess the frequency dependence of the gradient we attempted to filter higher frequencies from Ps conversions, and reinvert the data. However, Ps conversions from the lithosphere-asthenosphere boundary arrive very close to crustal reverberations, especially at station HRV. Therefore excluding higher frequencies causes interference between reverberations and the phase of interest, rather than revealing any information about the boundary.

[44] Alternatively, we assess the maximum difference in velocity gradient that can be expected for Ps and Sp phases owing to the frequency dependence of attenuation using the relationships for the anelastic regime (temperatures greater than ~950°C) developed by *Faul and Jackson* [2005] for attenuation (Q^{-1}) and shear velocity (V_s). We employ the experimental parameters given by *Faul and Jackson* [2005], and where choices exist we use the following parameter values for our model: the grain size, d = 1×10^{-3} m [*Evans et al.*, 2001]; density, $\rho = 3.37$ g/cm^3 [*Dziewonski and Anderson*, 1981; *Kennett and Engdahl*, 1991]; and pressure, P, at 100 km depth (3.1 GPa). The choice of grain size is conservative [*Evans et al.*, 2001], and increased grain sizes have the effect of decreasing the maximum difference in velocity contrast expected between Ps and Sp waves.

[45] We bound the maximum effects of attenuation by considering Q values (inverse attenuation) reported by global surface wave studies in regions of old oceanic lithosphere or continental shields, 56–105 in the lithosphere and 102–195 in the asthenosphere [*Dalton and Ekström*, 2006], using a period of 75 s, which has a peak sensitivity at ~100 km. Employing these parameter choices in the *Faul and Jackson* [2005] expression for Q limits the range of possible temperatures in the lithosphere and the asthenosphere. The *Faul and Jackson* [2005] relationships describe the effect of attenuation on velocity using temperature as the dominant physical variable. However, for our purposes they are simply a means of quantifying the effect of attenuation on phases at a given period. For example, attenuation could also be increased by the presence of water and still produce a similar frequency dependence [*Karato*, 2003]. Using the *Faul and Jackson* [2005] expression for shear modulus and the newly bounded effective temperatures we calculate the maximum differences between the Ps and Sp velocity
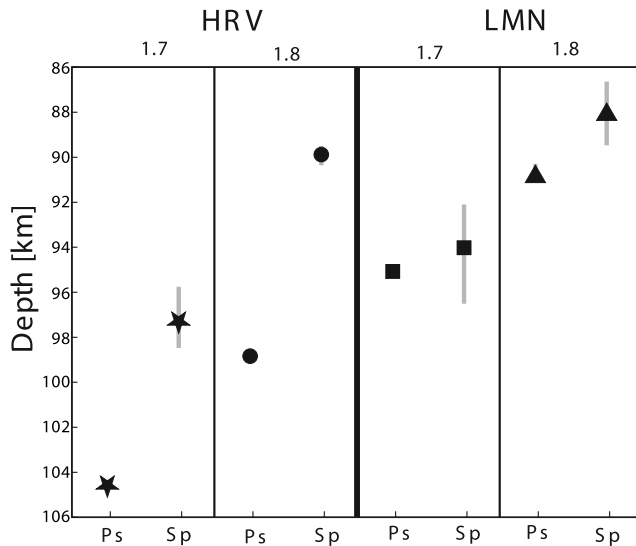
Figure 11. Discontinuity depths. The depths to which *Ps* and *Sp* conversions from the lithosphere-asthenosphere boundary migrate assuming $V_p/V_s = 1.7$ (stars for HRV and squares for LMN) are compared to the case where $V_p/V_s = 1.8$ is assumed (circles for HRV and triangles for LMN). For both models, assuming $V_p/V_s = 1.7$ and $V_p/V_s = 1.8$, *Sp* data at a given station require a shallower lithosphere-asthenosphere boundary depth than *Ps* data. However, the phases sample significantly different swaths of the mantle at the depth of the base of the lithosphere. The 95% error bars (grey lines) were determined by performing a grid search in depth and using an *F* test, as described in section 5.4. In the cases where no error bar is shown, the error bars are smaller than the symbol.

contrasts at the lithosphere-asthenosphere boundary given the dominant periods of the waveforms recorded at a station (see section 5.5).

[46] We find that the *Ps* velocity gradients could be slightly smaller than those of *Sp* (on the order of 0.5%) due to the inherently shorter periods of *Ps* relative to *Sp*. In light of the structure of our inversion results, including the possible effect of the frequency dependence of attenuation would only sharpen the required velocity gradient, since this parameter combination lies in a place just to the left of the true intersection points of the best fitting *Ps* and *Sp* models in Figure 9. Following the same logic, the depth over which the discontinuity occurs would be reduced by 0.8 km or less according to Figure 9. In the end, because the effects of frequency-dependent attenuation are small, and because we do not know how much of the velocity contrast is caused by an anelastic effect, we refer to the velocity gradients based on the simple intersections of the error bars in Figure 9 throughout the rest of this paper.

5.3. Depth to the Discontinuity

[47] We allow the depth to the discontinuity to vary in our inversions, but for a given conversion type (*Ps* or *Sp*) and V_p/V_s value at a given station, similar depths to the discontinuity (<0.2 km difference) are obtained for all best fitting models. However, *Sp* imaging indicates significantly shallower depths than *Ps* imaging at station HRV and slightly

shallower to similar values at LMN (Figure 11 and Table 2). At HRV the *Sp* lithosphere-asthenosphere boundary migrates to 89.5–90.4 km for $V_p/V_s = 1.8$ and 95.8–98.5 km for $V_p/V_s = 1.7$ versus 99 ± 0.1 km and 104.6 ± 0.1 km in the *Ps* data. At LMN the depth of the *Sp* lithosphere-asthenosphere boundary is 86.6–89.5 km for $V_p/V_s = 1.8$ and 92.1–96.5 km for $V_p/V_s = 1.7$ versus 91 ± 0.3 km and 95 ± 0.3 km in the *Ps* data.

5.4. Error Assessment at the Lithosphere-Asthenosphere Boundary

[48] To determine the error in velocity contrast at the lithosphere-asthenosphere boundary we perform grid searches in shear wave velocity drop where all other parameters are fixed at the previously determined best fitting model values for each gradient thickness and two different V_p/V_s values in the lithosphere and the asthenosphere (Figure 12). Exactly the same approach is applied to determine the error in the absolute depth of the lithosphere-asthenosphere boundary, but in this grid search all parameters are fixed except for the depth to which the discontinuity migrates. An *F* test is used to determine 95% confidence limits in velocity. We determine the number of degrees of freedom in the deconvolved, migrated phase from the lithosphere-asthenosphere boundary by inspecting different realizations of the phase, each with fewer points. The number of degrees of freedom is set as the fewest points required to retain the shape of the phase. We require 6 degrees of freedom to describe *Ps* phases and 7 degrees of freedom for *Sp* phases. We accept the velocity gradient model space where the *Ps* and *Sp* error bars overlap (section 5.2).

5.5. Dominant Periods of the Incident Waveforms

[49] Best fitting values for the dominant period of the incident waveform vary in a predictable though very small way in *Ps* models, decreasing as the thickness of the velocity gradient increases. Also, periods from the *Ps* models where $V_p/V_s = 1.7$ are slightly larger than those where $V_p/V_s = 1.8$ by up to 0.3 s. At HRV the best fitting periods range from 1.3 to 1.9 s. At LMN the best fitting *Ps* periods range from 2.9 to 3.8 s. The *Sp* periods vary very little as the thickness of the velocity gradient changes, by less than 0.4 s at HRV and LMN. The best fitting *Sp* periods at HRV range from 12.1 to 13.5 s, with larger periods corresponding to models where $V_p/V_s = 1.7$. At LMN the best fitting periods range from 7.8 to 8.4 s with the larger periods corresponding to models with $V_p/V_s = 1.8$. These periods are consistent with those determined by inspection of the original seismograms, and those calculated by autoconvolution of the source waveforms, *P* for *Ps* and *S* for *Sp*.

6. Discussion

6.1. Velocity Gradient at the Lithosphere-Asthenosphere Boundary

[50] Our new results combining inversions of *Ps* and *Sp* data reveal a velocity gradient at the lithosphere-asthenosphere boundary that is strong and sharp and in most respects comparable to the gradients inferred from *Ps* data alone [*Rychert et al.*, 2005]. At LMN the results for the magnitude and the thickness of the velocity gradient from the inversions agree very well, a 6.8–10.7% (*Ps*) versus a
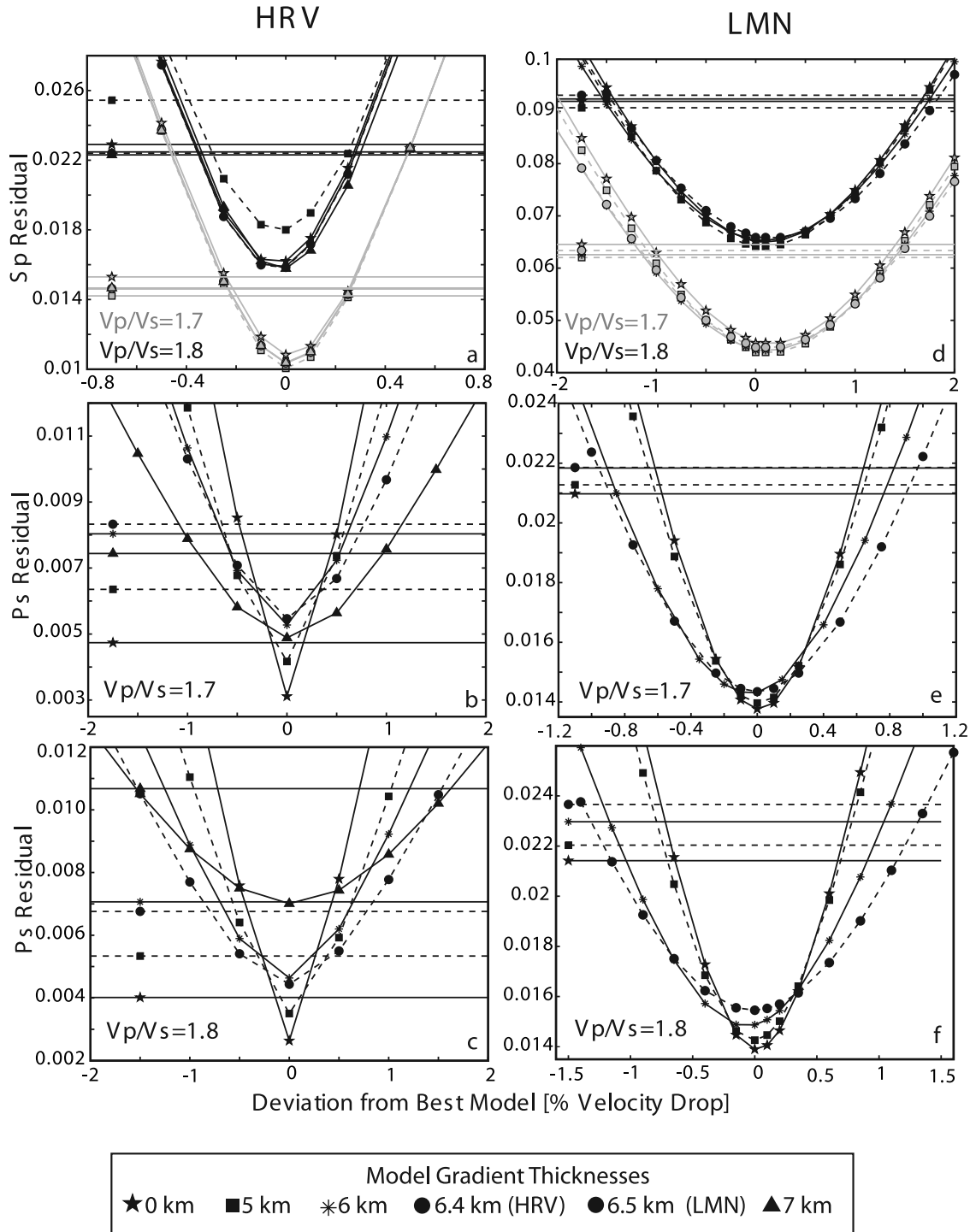
Figure 12. Error in the magnitude of the velocity drop. Curves represent the residuals for variations in the magnitude of the velocity drop from the best fitting models (deviation of 0%), holding all other parameters fixed. The straight lines represent the 95% confidence limits determined using an F test assuming 6 degrees of freedom in the Ps waveform and 7 degrees of freedom in the Sp waveform. The intersections of the 95% confidence limits with the corresponding residual curves provide the error bars determined at each gradient thickness for each model in Figure 9. HRV and LMN Sp residuals are shown in Figures 12a and 12d, respectively ($V_p/V_s = 1.7$ in grey and $V_p/V_s = 1.8$ in black), while Figures 12b (HRV) and 12e (LMN) represent Ps models with $V_p/V_s = 1.7$, and Figures 12c (HRV) and 12f (LMN) represent Ps models with $V_p/V_s = 1.8$.

6.0–9.6% (*Sp* and *Ps*) drop in shear wave velocity that occurs over 11 km or less (*Ps* alone and the combination of *Ps* and *Sp*). At HRV the new inversions that combine *Ps* and *Sp* information indicate a gradient thickness (5.2 to 6.4 km) that is similar to that obtained from *Ps* data alone (0–5 km). However, the addition of the *Sp* data does indicate a larger velocity drop (5.3–7.4%) than that inferred from the *Ps* data alone (3.1–4.9%), assuming no 61 km discontinuity.

[51] An explanation for this difference is that in our previous study, the trade-off between the gradient depth range and velocity drop was bounded using constraints on incident *P* wave period obtained by modeling the autode-convolved direct *P* phase [*Rychert et al.*, 2005], whereas in this study we constrain the trade-off using the overlap between *Sp* and *Ps* models. The results of the two approaches could be reconciled if the constraints on incident *P* wave period of *Rychert et al.* [2005] were mildly relaxed. Alternatively, both the inversion for *Ps* alone and that for *Ps* and *Sp* together could be accurate, indicating that the velocity gradient may change character from the region sampled by *Ps* to that sampled by *Sp*; *Sp* phases are converted at different locations and over much broader lateral area than *Ps* phases (Figures 1 and 2).

[52] Another possibility is that the differing velocity contrasts reflect a frequency-dependent response to attenuation (see section 5.2). If one assumes that the velocity drop partially reflects an increase in attenuation with depth consistent with observed global attenuation values [*Dalton and Ekström*, 2006], then accounting for the differing frequency content of the *Ps* and *Sp* phases could result in a *Ps* velocity contrast up to 0.5% smaller than that determined by combined *Ps*-*Sp*, with a gradient thickness up to 0.8 km thinner than those determined by the combined *Sp*-*Ps* inversions. Such an assumption regarding attenuation brings the gradient from the combined *Sp*-*Ps* inversions into agreement with the gradient determined by inversions of *Ps* alone at HRV, and may be evidence that a change in attenuation is at least partially responsible for the observed velocity contrast.

[53] The velocity drops determined for the entire region (i.e., HRV and LMN combined) by inverting *Ps* together with *Sp* data in this region (a 5–10% decrease) are within the range of the lid to low-velocity zone contrasts determined by surface wave studies in the region (3–11%) [*Li et al.*, 2003; *van der Lee*, 2002]. However, these surface wave studies cannot distinguish between sharp velocity contrasts and those that occur over up to ∼40–50 km. Other *Ps* studies of mantle discontinuities in this region do not observe a phase from depths comparable to base of the lithosphere at a common station, HRV [*Li et al.*, 2002; *Vinnik et al.*, 2005a]. However, the ability of the data in these studies to resolve a phase from the lithosphere-asthenosphere boundary is probably impeded by a lack of higher frequencies in the waveforms, which can cause interference with crustal phases.

[54] Our results are comparable to those obtained in another continental region, the Tanlu Fault Zone in eastern China where *Ps* data reveal a 3–7% velocity drop over a depth range of <10 km at 60–80 km depth [*Chen et al.*, 2006]. Similarly, *Sp* data in the Tien Shan suggest a strong discontinuity, a 6.7–8.9% drop in velocity that was assumed to occur as a single step function in depth [*Oreshin et*

al., 2002]. Reflection studies in localized zones at the base of the continental or passive margin lithosphere invoke gradients over comparable depth ranges [*Steer et al.*, 1998b], but they do not model the magnitude of the velocity drop. Finally, models for the base of old Pacific oceanic lithosphere using joint surface wave and body wave inversions (6.4%) over <30 km [*Gaherty et al.*, 1999] resemble our results.

6.2. Depth of the Lithosphere-Asthenosphere Boundary

[55] At LMN, the depth to which the *Sp* lithosphere-asthenosphere boundary migrates agrees well with the results from *Ps* modeling. *Sp* error bounds are as little as 2.6 km shallower than the *Ps* error bounds using $V_p/V_s = 1.8$, and boundary depths overlap for $V_p/V_s = 1.7$ (Figure 11 and Table 2).

[56] At HRV, the depth of the conversion associated with the lithosphere-asthenosphere boundary is shallower in the *Sp* imaging than the *Ps* imaging by at least 6 km (Figure 11 and Table 2). Both crustal structure and the V_p/V_s value of the lithosphere affect the depth to which the converted phase migrates. However, we have good constraints on the structure of the crust from inverting *Ps* data, and altering V_p/V_s is only a minimally effective way of reconciling the difference between the depths to which *Ps* and *Sp* migrate.

[57] The reason why V_p/V_s is not an effective way of reconciling depth differences between *Ps* and *Sp* lies in a trade-off within the migration process, which accounts for both the incidence angle of the ray in the lithosphere, and thus the travel distance to the surface, as well as the more obvious difference in *P* wave and *S* wave traveltimes owing to velocity. For fixed arrival times, an increase in V_p/V_s in the migration model assumes that *Ps* phases travel in a more vertical path, and *Sp* phases travel in a more horizontal path; this part of the calculation has the effect of moving *Ps* and *Sp* phases to deeper and shallower depths, respectively. However, increasing migration model V_p/V_s also assumes *S* wave velocity gets slower in relationship to a fixed *P* wave velocity; this part of the calculation has the effect of moving *Ps* and *Sp* phases to shallower and deeper depths, respectively. In the end, the effect of velocity dominates in *Ps* migration, and the effect of angle, or travel distance, dominates in *Sp* migration. The magnitude of the effect of changing V_p/V_s is not necessarily the same for *Ps* and *Sp* phases, and therefore small depth differences between *Ps* and *Sp* (∼2–3 km) may be reconciled by adjusting V_p/V_s. However, since a variation in V_p/V_s causes *Ps* and *Sp* phases to move in depth in the same direction, it is a relatively ineffective way of reconciling large depth differences between the phases (Figure 11).

[58] Even though V_p/V_s variations cannot reconcile the *Sp* and *Ps* lithosphere-asthenosphere boundary depths at HRV, the different discontinuity depths implied by the *Sp* and *Ps* data at HRV are not necessarily physically inconsistent. *Sp* samples the lithosphere-asthenosphere boundary in a circular band ∼100 to ∼800 km away from the station, while *Ps* samples it in a band ∼20 to ∼30 km away from the station. In this distance range either the depth to the discontinuity or the lithospheric V_p/V_s value could easily vary. If *Ps* and *Sp* experience different V_p/V_s values, then this parameter is an effective way of reconciling *Ps* and *Sp* depths.

[59] Indeed, the only region of direct conflict of *Sp* with *Ps* depths is in the northwestern area of the study region where *Ps* phases from LBNH image a deep lithosphere-asthenosphere boundary at 110 km, whereas *Sp* waveforms recorded at HRV but converted near LBNH image a shallower discontinuity (Figure 2). We investigated the possibility that *Ps* variations in the region could be matched by *Sp*, by back-azimuthally binning *Sp* data recorded at HRV. Though the reduced quantity of data in back-azimuthally binned waveforms decreases the quality, these results do not suggest a deeper lithosphere-asthenosphere boundary for events from the northwest. In fact, we have more *Sp* phases from back azimuths of 315°−335° than in any other back-azimuthal bin, and these data closely resemble the signal for the complete *Sp* data set that we model.

[60] However, another consideration is that the *Ps* phase at LBNH that we interpreted as representing the lithosphere-asthenosphere boundary is the weakest and least clear among the *Ps* data modeled in the work of *Rychert et al.* [2005], and it is possible that the depth to the lithosphere-asthenosphere discontinuity beneath LBNH is not as deep as previously believed. Because we are not able to distinguish between these two possibilities, we do not include the piercing points of LBNH and northwestern HRV data in our interpolated surface of the lithosphere-asthenosphere boundary in Figure 2.

[61] The depth of the conversion from the lithosphere-asthenosphere boundary in both *Ps* and *Sp* imaging (Figure 11) agrees well the base of the fast lid observed by surface waves in this region (60−100 km at HRV [*Li et al.*, 2003] and 50−90 km depth at LMN [*van der Lee*, 2002]) (Figure 3), defined by the sharpest section of a larger, more gradual velocity drop. In fact, all *Ps* and *Sp* models at HRV and LMN assuming $V_p/V_s = 1.8$ fall within the depth range of the base of the fast lid determined by surface waves.

6.3. Which V_p/V_s?

[62] Standard global 1-D velocity models include $V_p/V_s = 1.8$ in the shallow mantle [*Dziewonski and Anderson*, 1981; *Kennett and Engdahl*, 1991]. However, we also performed inversions using V_p/V_s values of 1.7−1.9 to test the V_p/V_s sensitivities of our inferred lithosphere-asthenosphere velocity gradients. The gradient parameters (thickness and magnitude) are not very sensitive to V_p/V_s (Figure 9). We also find that the fit to the *Ps* and *Sp* waveforms is not in general significantly improved by one V_p/V_s value versus another (for example, see Figure 12). There is better agreement in the depth to which the phase from the lithosphere-asthenosphere boundary migrates between *Ps* and *Sp* models at both stations HRV and LMN when $V_p/V_s = 1.7$ is assumed (Figure 11), but since *Sp* and *Ps* data sample different regions of the mantle (Figures 1 and 2), differences in the depth to the discontinuity using *Ps* and *Sp* might be real. Finally, the depth of the lithosphere-asthenosphere boundary in models with $V_p/V_s = 1.8$ agree better with the depth of the fast velocity lid in surface wave studies [*Li et al.*, 2003; *van der Lee*, 2002]. Overall, our results do not shed light on the preferred V_p/V_s value for the mantle.

6.4. The Crust

[63] We did not invert *Sp* data for crustal parameters. However, the depths to which *Sp* crustal phases migrate, using the best fitting *Ps* models for migration, agree well those determined by *Ps* inversions. At HRV, *Ps* inversions indicate a 30.2 ± 0.3 km thick crust (crustal $V_p/V_s = 1.68$), which is the same depth that the direct crustal arrival migrates to in the *Sp* data. Also, the crustal results from *Ps* and *Sp* agree well with another *Ps* receiver function study at HRV which found a 30 km thick crust with a V_p/V_s of 1.67 [*Ramesh et al.*, 2002]. Inversions of *Ps* data at LMN find a 41 ± 2 km thick crust (crustal $V_p/V_s = 1.65$), which is slightly larger than the depth to which the peak of the *Sp* Moho phase migrates, 36 km assuming the same crustal V_p/V_s. However, the discrepancy in depth is not very significant given the width of the phase. Overall, *Sp* has less ability to resolve fine-scale crustal structure owing to its inherently longer dominant period [*Sodoudi et al.*, 2006]. If differences between *Ps* and *Sp* models for the crust do reflect real structure, one explanation for the discrepancy is that *Sp* phases sample discontinuities at different lateral locations than *Ps* due to different raypaths, ∼32−52 km versus ∼7−12 km away from LMN, respectively. Another possibility is that our *Sp* and *Ps* results at LMN are different due to anisotropy in the crust. Another study of crustal structure at LMN reported a possible anisotropic lower crust, with a Moho depth at 42−50 km [*Bank and Bostock*, 2003]. Such anisotropy may be complicating our results, especially since *Ps* modeling at LMN only considered events from the west [*Rychert et al.*, 2005], but events from all back azimuths were considered for the *Sp* modeling.

7. Mechanisms for a Strong, Sharp Velocity Gradient

[64] Several physical and chemical factors affect seismic velocities including thermal gradients, grain size, chemical depletion due to melting, water content, and melt content. We test the combination of these parameters that might be responsible for our observed velocity gradient, starting with gradients produced by purely thermal models.

7.1. Purely Thermal Gradients

[65] Thermal gradients certainly must make a contribution to our observed velocity gradient. However, here we test whether our velocity gradient may be described by thermal processes alone. To do this, we calculate the minimum temperature gradients required to explain the minimum velocity contrasts, a 5.3% contrast at HRV and a 6.0% contrast at LMN, and the maximum gradient thicknesses, 6 km at HRV and 11 km at LMN. Note that although accounting for frequency dependence would decrease the magnitude of the velocity gradient required for *Ps*, it would also sharpen the required velocity gradient (see section 5.2), and therefore our parameter choices remain conservative.

[66] We evaluate the minimum required temperature gradient using two approaches. In the first, we follow experimental studies that suggest that if the observed velocity gradient is caused solely by temperature it can be described using an experimentally derived relationship of shear velocity to temperature and pressure [*Faul and Jackson*, 2005]. We choose conservative parameter values, including the maximum periods from our inversions, i.e., those of *Sp* models, and minimum grain size values (1 mm)

[*Evans et al.*, 2001] to estimate the smallest required thermal contrast to explain our modeled velocity gradients. Using the rest of the parameter choices described in section 5.2, temperature increases of at least 227°C and 199°C are required to explain the maximum velocity contrasts at LMN and HRV, respectively. As in the case of our previous *Ps* study, a large thermal gradient, here greater than 21°C/km, would be required if the velocity contrast were purely thermal. We also tested this calculation using the earlier attenuation-temperature and velocity-attenuation relationships of *Jackson et al.* [2002] and *Karato* [2003] using the same parameter choices described above for period and grain size, a conservative activation volume (V = 6 × 10^{-6} m³/mol) at the lower end of experimentally determined values [*Hirth and Kohlstedt*, 2003], and other experimentally determined parameter values [*Jackson et al.*, 2002] (also described by *Rychert et al.* [2005]). We find temperature contrasts of 167°C and 133°C are required to explain the maximum velocity contrasts at LMN and HRV, or >15°C/km.

[67] In our second approach, we use an empirical relationship between shear wave velocity and temperature which is independent of grain size and frequency [*Priestley and McKenzie*, 2006]. The relationship was developed by combining thermal models of Pacific lithosphere, pressure and temperature estimates from kimberlites, and V_s from surface waves. We find that thermal contrasts of at least 225° and 345° are required to explain the velocity contrasts observed at HRV and LMN, respectively (we assume the temperature of the sublithospheric asthenosphere is 1375°C).

[68] All of these approaches provide thermal gradients of at least 15°C/km. In numerical models of flow and thermal structure at the base of the continental lithosphere in which viscosity depends on temperature and pressure but is not affected by composition, thermal gradients at the base of the lithosphere are typically less than 5°C/km, and definitely less than 10°C/km [*King and Ritsema*, 2000; *Zaranek et al.*, 2005]. Therefore we conclude that another mechanism besides temperature is required to explain the observed velocity contrast.

7.2. Combining Temperature and Composition

[69] A vertical variation in depletion could be responsible for a sharp velocity contrast with a magnitude of up to ~0.9% [*Schutt and Lesher*, 2006] or ~1.5% [*Lee*, 2003]. Similarly, a transition from a dehydrated lithosphere to a hydrated asthenosphere [*Gaherty et al.*, 1999; *Hirth and Kohlstedt*, 1996; *Hirth et al.*, 2000; *Karato and Jung*, 1998] could easily produce a sharp enough boundary. Assuming that water affects velocity via attenuation [*Karato*, 2003; *Karato and Jung*, 1998], and following the equations, parameters, and logic of section 5.2, a dehydration boundary may account for a velocity drop of up to 3.8% at HRV and LMN. Note that this value may not be expanded by including the effects of temperature because it is already limited by global ranges of observed attenuation [*Dalton and Ekström*, 2006]. While the effects of water alone are insufficient to explain the 5.3% and 6.0% minimum velocity contrasts required by our combined *Sp-Ps* inversions at stations HRV and LMN, respectively, the combination of

a boundary in depletion [*Lee*, 2003; *Schutt and Lesher*, 2006] and dehydration satisfies our minimum velocity gradient at HRV, and comes close to matching the observations at LMN. Therefore we accept a boundary in dehydration and depletion as an explanation for the observed velocity gradients, particularly given that experimental constraints on the effect of water on seismic velocities are at an early stage.

[70] Like water, grain size affects velocity through attenuation [*Faul and Jackson*, 2005; *Jackson et al.*, 2002]. Therefore the total effect of water and grain size on velocity is also limited by globally observed values of attenuation [*Dalton and Ekström*, 2006] to be <3.8%. However, it is unlikely that a combination of grain size and temperature is responsible for our observed boundary. Grain size is inversely proportional to stress [*Karato et al.*, 1980; *Twiss*, 1977; *Van der Wal et al.*, 1993], and therefore a very sharp increase in shear stress with depth would be required to produce the velocity gradients at HRV and LMN. However, numerical modeling indicates that shear stress generally decreases gradually with depth for the case in which viscosity depends only on temperature and pressure [*Zaranek et al.*, 2005].

7.3. Contributions From Anisotropy

[71] An apparent drop in velocity could be created by a change in the strength or orientation of anisotropy. Here we explore cases where no change in average isotropic velocity occurs in order to isolate contributions from anisotropy relative to other mechanisms.

[72] Models containing vertical changes in azimuthal anisotropy strong enough to produce the observed lithosphere-asthenosphere boundary phases should also produce significant variations in phase amplitude as a function of back azimuth. For olivine with a horizontal *a* axis, the largest *Ps* amplitude variations are for back azimuths 90° apart. The *Ps* data from HRV has the best back-azimuthal distribution of events, and although breaking the data into back-azimuthal bins leads to noisier signals, clear lithosphere-asthenosphere boundary phases are observed for the three back-azimuthal bins with the most data (roughly 180°, 315°, and 330°). All of these phases are negative and their amplitudes vary by less than a factor of 2.5. Given these amplitudes and a horizontal *a* axis, at least 70% of the velocity drop at HRV must be due to a reduction in the isotropic component of mantle velocity rather than a rotation or increase in anisotropic alignment.

[73] A vertical change in radial anisotropy could also contribute to the velocity drop at the lithosphere-asthenosphere boundary, and in this case no azimuthal variations in phase amplitudes would be predicted. Examples include a shift from isotropy in the lithosphere to radial anisotropy in the asthenosphere with a slow horizontal plane (and fast vertical symmetry axis), or stronger radial anisotropy in the lithosphere with a fast horizontal plane (and slow vertical symmetry axis). However, vertical stretching or shearing in the asthenosphere seems unlikely over such a broad region, and while past deformation is difficult to constrain, there is no obvious mechanism to emplace a fast horizontal plane in the lithosphere that is uniform at the scale sampled by the scattered waves. In addition, there is no clear evidence for a

sharp change in radial anisotropy in this depth range in surface wave models for this region [*Gaherty*, 2004]. Although subtle changes in radial anisotropy over small depth intervals could be missed by long-period surface waves, variations in radial anisotropy large enough to produce an apparent velocity drop of 5–10% should be apparent, albeit in a smoothed manner. Furthermore, even if a vertical variation in radial anisotropy exists, somehow missed by surface waves, then a mechanism for producing a change in anisotropy over less than 11 km would still be required. If anisotropy reflects present-day deformation, this brings us back to the need for the presence of water and/or melt in the asthenosphere.

[74] Overall, while anisotropy is not a likely explanation for the total magnitude of our observed velocity gradient, it could be responsible for a portion of the velocity drop if it works in concert with another mechanism such as a boundary in hydration, depletion, or melt.

7.4. Contributions From Partial Melt

[75] Alternatively, the strong, sharp lithosphere-asthenosphere boundary may be produced by the presence of small amounts of partial melt in the asthenosphere [*Anderson*, 1989; *Mierdel et al.*, 2007]. Our range of inversion results for the velocity gradient at the lithosphere-asthenosphere boundary may be explained by the presence of partial melt in the asthenosphere at levels of 1.2–1.4% (HRV) and 1.3–1.7% (LMN) [*Hammond and Humphreys*, 2000] or 2.7%–3.8% (HRV) and 3.0–4.9% (LMN) [*Kreutzmann et al.*, 2004]. In this scenario, the lithosphere-asthenosphere boundary would be defined by the solidus, causing melt to refreeze as it rises into the lithosphere. For peridotite solidi corresponding to a mildly hydrated asthenosphere, 800–1000 $H/10^6$ Si [*Hirth and Kohlstedt*, 1996], a range of reasonable mantle temperatures will be above the solidus at asthenospheric depths, and will cross to temperatures below the solidus at the depths we infer for the lithosphere-asthenosphere boundary.

[76] One possible model for generating melt in the asthenosphere beneath eastern North America would be decompression of mildly hydrated asthenospheric material related to the shape of the rigid, shallowing lithosphere as it moves in the WSW direction [*Fouch et al.*, 2000; *Zaranek et al.*, 2005]. Alternatively, mantle temperatures may exceed the solidus within the asthenosphere without the need for decompression [e.g., *Anderson*, 1989]. It has recently been suggested that a sharp decrease in water solubility in aluminous orthopyroxene with depth, coupled with the far more gradual increase in water solubility in olivine, will promote melting just below the base of the lithosphere [*Mierdel et al.*, 2007].

8. Conclusions

[77] Both *Ps* and *Sp* converted energy independently confirm the existence of a discontinuity that correlates with the lithosphere-asthenosphere boundary at 87–105 km depth in eastern North America.

[78] Both *Ps* and *Sp* waveforms are mainly sensitive to changes in shear wave velocity, but the different information in *Ps* and *Sp* phases can be used to constrain the properties of velocity gradients. *Ps* amplitudes exhibit greater sensitivity to the thickness of velocity gradients than *Sp* because *P* waves exhibit inherently shorter dominant periods than *S* waves. If a boundary is produced in part by frequency-dependent attenuation, *Ps* velocity contrasts may appear to be slightly smaller than those of *Sp*, but overall the difference is small in our results. Varying the mantle-lithospheric V_p/V_s value assumed in a one-dimensional migration model can reconcile only small differences, up to ∼2.5 km, between the migrated depths of *Ps* and *Sp* conversions from the base of the lithosphere. However, larger differences in *Ps* and *Sp* depths at a single station may reflect lateral variations in discontinuity properties given that *Ps* and *Sp* sample significantly different regions at the depth of the lithosphere-asthenosphere boundary.

[79] The combination of *Ps* and *Sp* inversions requires that the lithosphere-asthenosphere boundary in eastern North America is strong, a 5–10% velocity drop, and sharp, occurring over less than 11 km depth. Such a strong, sharp velocity gradient requires another mechanism beyond a purely thermal gradient to define the lithosphere-asthenosphere boundary. One explanation is that the boundary is defined by a transition from a dehydrated lithosphere to a weaker asthenosphere in concert with a boundary in depletion and/or a change in anisotropic signature. Another possibility is that the asthenosphere in this region contains a small amount of partial melt.

References

Aki, K., and P. G. Richards (1980), *Quantitative Seismology: Theory and Methods*, W. H. Freeman, San Francisco, Calif.

Ammon, C. J., G. E. Randall, and G. Zandt (1990), On the nonuniqueness of receiver function inversions, *J. Geophys. Res.*, *95*(B10), 15,303–15,318.

Anderson, D. L. (1989), *Theory of the Earth*, 366 pp., Blackwell Sci., Boston, Mass.

Bank, C., and M. G. Bostock (2003), Linearized inverse scattering of teleseismic waves for anisotropic crust and mantle structure: 2. Numerical examples and application to data from Canadian stations, *J. Geophys. Res.*, *108*(B5), 2259, doi:10.1029/2002JB001951.

Bostock, M. G. (1998), Mantle stratigraphy and evolution of the Slave province, *J. Geophys. Res.*, *103*(B9), 21,183–21,200.

Bostock, M. G. (1999), Seismic waves converted from velocity gradient anomalies in the Earth's upper mantle, *Geophys. J. Int.*, *138*, 747–756.

Chen, L., T. Zheng, and W. Xu (2006), A thinned lithospheric image of the Tanlu Fault Zone, eastern China: Constructed from wave equation based receiver function migration, *J. Geophys. Res.*, *111*, B09312, doi:10.1029/2005JB003974.

Collins, J. A., F. L. Vernon, J. A. Orcutt, R. A. Stephen, K. R. Peal, F. B. Wooding, F. N. Spiess, and J. A. Hildebrand (2001), Broadband seismology in the oceans; lessons from the ocean seismic network pilot experiment, *Geophys. Res. Lett.*, *28*(1), 49–52.

Dalton, C. A., and G. Ekström (2006), Global models of surface wave attenuation, *J. Geophys. Res.*, *111*, B05317, doi:10.1029/2005JB003997.

Dziewonski, A. M., and D. L. Anderson (1981), Preliminary reference Earth model, *Phys. Earth Planet. Inter.*, *25*(4), 297–356.

Evans, B., J. Renner, and G. Hirth (2001), A few remarks on the kinetics of static grain growth in rocks, *Int. J. Earth Sci.*, *90*, 88–103, doi:10.1007/s005310000150.

Farra, V., and L. Vinnik (2000), Upper mantle stratification by *P* and *S* receiver functions, *Geophys. J. Int.*, *141*, 699–712.

Faul, U. H., and I. Jackson (2005), The seismological signature of temperature and grain size variations in the upper mantle, *Earth Planet. Sci. Lett.*, *234*(1–2), 119–134.

Fouch, M. J., K. M. Fischer, E. M. Parmentier, M. E. Wysession, and T. J. Clarke (2000), Shear wave splitting, continental keels, and patterns of mantle flow, *J. Geophys. Res.*, *105*(B3), 6255–6275.

Gaherty, J. B. (2004), A surface wave analysis of seismic anisotropy beneath eastern North America, *Geophys. J. Int.*, *158*, 1053–1066.

Gaherty, J. B., M. Kato, and T. H. Jordan (1999), Seismological structure of the upper mantle; a regional comparison of seismic layering, *Phys. Earth Planet. Inter.*, *110*(1–2), 21–41.

Hammond, W. C., and E. D. Humphreys (2000), Upper mantle seismic wave velocity: Effects of realistic partial melt geometries, *J. Geophys. Res.*, *105*(B5), 10,975–10,986.

Hatcher, R. D., Jr. (1989), Tectonic synthesis of the U.S. Appalachians, in *The Appalachian-Ouachita Orogen in the United States.*, edited by R. D. Hatcher Jr., W. A. Thomas, and G. W. Viele, pp.511–519, Geol. Soc. of Am., Boulder, Colo.

Heaman, L. M., and B. A. Kjarsgaard (2000), Timing of eastern North American kimberlite magmatism; continental extension of the Great Meteor hotspot track?, *Earth Planet. Sci. Lett.*, *178*(3–4), 253–268.

Hirth, G., and D. L. Kohlstedt (1996), Water in the oceanic upper mantle; implications for rheology, melt extraction and the evolution of the lithosphere, *Earth Planet. Sci. Lett.*, *144*(1–2), 93–108.

Hirth, G., and D. L. Kohlstedt (2003), Rheology of the upper mantle and the mantle wedge: A view from the experimentalists, in *Inside the Subduction Factory, Geophys. Monogr. Ser.*, vol. 138, edited by J. Eiler, pp.83–105, AGU, Washington, D. C.

Hirth, G., R. L. Evans, and A. D. Chave (2000), Comparison of continental and oceanic mantle electrical conductivity: Is the Archean lithosphere dry?, *Geochem. Geophys. Geosyst.*, *1*(12), doi:10.1029/2000GC000048.

Jackson, I., J. D. Fitz Gerald, U. H. Faul, and B. H. Tan (2002), Grain-size-sensitive seismic wave attenuation in polycrystalline olivine, *J. Geophys. Res.*, *107*(B12), 2360, doi:10.1029/2001JB001225.

Karato, S.-I., (2003), Mapping water content in the upper mantle, in *Inside the Subduction Factory, Geophys. Monogr. Ser.*, vol. 138, edited by J. Eiler, pp.135–152, AGU, Washington, D. C.

Karato, S.-I., and H. Jung (1998), Water, partial melting and the origin of the seismic low velocity and high attenuation zone in the upper mantle, *Earth Planet. Sci. Lett.*, *157*(3–4), 193–207.

Karato, S.-I., M. Toriumi, and T. Fujii (1980), Dynamic recrystallization of olivine single crystals during high-temperature creep, *Geophys. Res. Lett.*, *7*(9), 649–652.

Keith, C. M., and S. Crampin (1977), Seismic body waves in anisotropic media: Synthetic seismograms, *Geophys. J. R. Astron. Soc.*, *49*(1), 225–243.

Kennett, B. L. N., and E. R. Engdahl (1991), Traveltimes for global earthquake location and phase identification, *Geophys. J. Int.*, *105*, 429–465.

King, S. D., and J. Ritsema (2000), African hot spot volcanism: Small scale convection in the upper mantle beneath cratons, *Science*, *290*, 1137–1140.

Kreutzmann, A., H. Schmeling, A. Junge, T. Ruedas, G. Marquart, and I. T. Bjarnason (2004), Temperature and melting of a ridge-centred plume with application to Iceland. Part II: Predictions for electromagnetic and seismic observables, *Geophys. J. Int.*, *159*, 1097–1111.

Kumar, P., et al. (2005a), The lithosphere-asthenosphere boundary in the North-West Atlantic region, *Earth Planet. Sci. Lett.*, *236*(1–2), 249–257, doi:10.1016/j.epsl.2005.05.029.

Kumar, P., X. Yuan, R. Kind, and G. Kosarev (2005b), The lithosphere-asthenosphere boundary in the Tien Shan-Karakoram region from S receiver functions: Evidence for continental subduction, *Geophys. Res. Lett.*, *32*, L07305, doi:10.1029/2004GL022291.

Kumar, P., X. Yuan, R. Kind, and J. Ni (2006), Imaging the colliding Indian and Asian lithospheric plates beneath Tibet, *J. Geophys. Res.*, *111*, B06308, doi:10.1029/2005JB003930.

Lee, C. A. (2003), Compositional variation of density and seismic velocities in natural peridotites at STP conditions: Implications for seismic imaging of compositional heterogeneities in the upper mantle, *J. Geophys. Res.*, *108*(B9), 2441, doi:10.1029/2003JB002413.

Li, A., K. M. Fischer, S. van der Lee, and M. E. Wysession (2002), Crust and upper mantle discontinuity structure beneath eastern North America, *J. Geophys. Res.*, *107*(B5), 2100, doi:10.1029/2001JB000190.

Li, A., D. W. Forsyth, and K. M. Fischer (2003), Shear velocity structure and azimuthal anisotropy beneath eastern North America from Rayleigh wave inversion, *J. Geophys. Res.*, *108*(B8), 2362, doi:10.1029/2002JB002259.

Li, X., R. Kind, K. Priestley, S. V. Sobolev, F. Tilmann, X. Yuan, and M. Weber (2000), Mapping the Hawaiian plume conduit with converted seismic waves, *Nature*, *405*(6789), 938–941.

Li, X., R. Kind, X. Yuan, I. Woelbern, and W. Hanka (2004), Rejuvenation of the lithosphere by the Hawaiian Plume, *Nature*, *427*(6977), 827–829.

Mierdel, K., H. Keppler, J. R. Smyth, and L. Falko (2007), Water solubility in aluminous orthopyroxene and the origin of Earth's asthenosphere, *Science*, *315*, 364–368, doi:10.1126/science.1135422.

Mohsen, A., R. Kind, S. V. Sobolev, M. Weber, and the DESERT Group (2006), Thickness of the lithosphere east of the Dead Sea Transform, *Geophys. J. Int.*, *167*, 845–852, doi:10.1111/j.1365-246X.2006.03185.x.

MONA LISA Working Group (1997), MONA LISA—Deep seismic investigations of the lithosphere in the southeastern North Sea, *Tectonophysics*, *269*, 1–19.

Morozova, E. A., I. B. Morozov, S. B. Smithson, and L. N. Solodilov (1999), Heterogeneity of the uppermost mantle beneath Russian Eurasia from the ultra-long-range profile QUARTZ, *J. Geophys. Res.*, *104*(B9), 20,329–20,348.

Musacchio, G., W. D. Mooney, J. H. Luetgert, and N. I. Christensen (1997), Composition of the crust in the Grenville and Appalachian provinces of North America inferred from V_P/V_S ratios, *J. Geophys. Res.*, *102*(B7), 15,225–15,242.

Oreshin, S., L. Vinnik, D. Peregoudov, and S. Roecker (2002), Lithosphere and asthenosphere of the Tien Shan imaged by S receiver functions, *Geophys. Res. Lett.*, *29*(8), 1191, doi:10.1029/2001GL014441.

Priestley, K., and D. McKenzie (2006), The thermal structure of the lithosphere from shear wave velocities, *Earth Planet. Sci. Lett.*, *244*(1–2), 285–301, doi:10.1016/j.epsl.2006.01.008.

Ramesh, D. S., R. Kind, and X. Yuan (2002), Receiver function analysis of the North American crust and upper mantle, *Geophys. J. Int.*, *150*, 91–108.

Revenaugh, J., and T. H. Jordan (1991), Mantle layering from ScS reverberations: 3. The upper mantle, *J. Geophys. Res.*, *96*(B12), 19,781–19,810.

Revenaugh, J., and S. A. Sipkin (1994), Mantle discontinuity structure beneath China, *J. Geophys. Res.*, *99*(B11), 21,911–21,927.

Richards, P. G. (1972), Seismic waves reflected from velocity gradient anomalies within the Earth's upper mantle, *J. Geophys.*, *38*, 517–527.

Ryberg, T., F. Wenzel, J. Mechie, A. Egorkin, K. Fuchs, and L. Solodilov (1996), Two-dimensional velocity structure beneath northern Eurasia derived from the super long-range seismic profile Quartz, *Bull. Seismol. Soc. Am.*, *86*(3), 857–867.

Rychert, C. A., K. M. Fischer, and S. Rondenay (2005), A sharp lithosphere-asthenosphere boundary imaged beneath eastern North America, *Nature*, *436*, 542–545, doi:10.1038/nature03904.

Schutt, D. L., and C. E. Lesher (2006), Effects of melt depletion on the density and seismic velocity of garnet and spinel lherzolite, *J. Geophys. Res.*, *111*, B05401, doi:10.1029/2003JB002950.

Shearer, P. M. (1991), Constraints on upper mantle discontinuities from observations of long-period reflected and converted phases, *J. Geophys. Res.*, *96*(B11), 18,147–18,182.

Sodoudi, F., X. Yuan, Q. Liu, R. Kind, and J. Chen (2006), Lithospheric thickness beneath the Dabie Shan, central eastern China from S receiver functions, *Geophys. J. Int.*, *166*, 1363–1367, doi:10.111/j.1365-246X.2006.03080.x.

Steer, D. N., J. H. Knapp, and D. L. Brown (1998a), Super-deep reflection profiling: Exploring the continental mantle lid, *Tectonophysics*, *286*, 111–121.

Steer, D. N., J. H. Knapp, L. D. Brown, H. P. Echtler, D. L. Brown, and R. Berzin (1998b), Deep structure of the continental lithosphere in an unextended orogen: An explosive source seismic reflection profile in the Urals (Urals Seismic Experiment and Integrated Studies (URSEIS 1995)), *Tectonics*, *17*(2), 143–157.

Thybo, H., and E. Perchuc (1997), The seismic 8° discontinuity and partial melting in continental mantle, *Science*, *275*, 1626–1629.

Twiss, R. J. (1977), Theory and applicability of a recrystallized grain size paleopiezometer, *Pure Appl. Geophys.*, *115*, 227–244.

van der Lee, S. (2002), High-resolution estimates of lithospheric thickness from Missouri to Massachusetts, *USA, Earth Planet. Sci. Lett.*, *203*(1), 15–23.

van der Lee, S., H. Paulssen, and G. Nolet (1994), Variability of P660S phases as a consequence of topography, *Phys. Earth Planet. Inter.*, *86*(1–3), 147–164.

Van der Wal, D., P. Chopra, M. Drury, and J. Fitz Gerald (1993), Relationships between dynamically recrystallised grain size and deformation conditions in experimentally deformed olivine rocks, *Geophys. Res. Lett.*, *20*, 1479–1482.

Vinnik, L., and V. Farra (2002), Subcratonic low-velocity layer and flood basalts, *Geophys. Res. Lett.*, *29*(4), 1049, doi:10.1029/2001GL014064.

Vinnik, L., M. Ravi Kumar, R. Kind, and V. Farra (2003), Super-deep low-velocity layer beneath the Arabian plate, *Geophys. Res. Lett.*, *30*(7), 1415, doi:10.1029/2002GL016590.

Vinnik, L. P., V. Farra, and R. Kind (2004a), Deep structure of the Afro-Arabian hotspot by S receiver functions, *Geophys. Res. Lett.*, *31*, L11608, doi:10.1029/2004GL019574.

Vinnik, L. P., C. Reigber, I. Aleshin, G. L. Kosarev, M. K. Kaban, S. I. Oreshin, and S. W. Roecker (2004b), Receiver function tomography of the central Tien Shan, *Earth Planet. Sci. Lett.*, *225*, 131–146.

Vinnik, L., E. Kurnik, and V. Farra (2005a), Lehmann discontinuity beneath North America: No role for seismic anisotropy, *Geophys. Res. Lett.*, *32*, L09306, doi:10.1029/2004GL022333.

Vinnik, L. P., G. R. Foulger, and Z. Du (2005b), Seismic boundaries in the mantle beneath Iceland: A new constraint on temperature, *Geophys. J. Int.*, *160*, 533–538.

Wilson, D., S. Grand, D. Angus, and J. Ni (2006), Constraints on the interpretation of S-to-P receiver functions, *Geophys. J. Int.*, *165*(3), 969–980, doi:10.1111/j.1365-246X.2006.02981.x.

Yuan, X., R. Kind, X. Li, and R. Wang (2006), The S receiver functions: Synthetics and data example, *Geophys. J. Int.*, *165*, 555–564.

Zaranek, S. E., E. M. Parmentier, and K. M. Fischer (2005), Roles of small-scale convection, crustal heating, and basal motions in the evolution of the subcratonic lithosphere, *Eos Trans. AGU*, *86*(52), Fall Meet. Suppl., Abstract T22C-05.

Zhu, L. P., and H. Kanamori (2000), Moho depth variation in southern California from teleseismic receiver functions, *J. Geophys. Res.*, *105*(B2), 2969–2980.

————————————

K. M. Fischer, Department of Geological Sciences, Brown University, Box 1846, Providence, RI 02912, USA.

S. Rondenay, Department of Earth, Atmospheric, and Planetary Sciences, Massachusetts Institute of Technology, 77 Massachusetts Avenue, Cambridge, MA 02139, USA.

C. A. Rychert, Institute of Geophysics and Planetary Physics, Scripps Institution of Oceanography, University of California, San Diego, 9500 Gilman Drive, La Jolla, CA 92093-0225, USA. (crychert@ucsd.edu)